Lithos 346–347 (2019) 105147

Contents lists available at ScienceDirect

Lithos

journal homepage: www.elsevier.com/locate/lithos

Proto-Tethys oceanic slab break-off: Insights from early Paleozoic magmatic diversity in the West Kunlun Orogen, NW Tibetan Plateau

Qichao Zhang [a,*], Zhenhan Wu [a], Xuanhua Chen [a], Qing Zhou [b], Nengping Shen [c]

[a] Chinese Academy of Geological Sciences, Beijing 100037, China
[b] Chengdu Institute of Geology and Mineral Resources, Chinese Geological Survey, Chengdu 610081, PR China
[c] State Key Laboratory of Ore Deposit Geochemistry, Institute of Geochemistry, Chinese Academy of Sciences, Guiyang 550081, China

ARTICLE INFO

Article history:
Received 12 February 2019
Received in revised form 10 July 2019
Accepted 11 July 2019
Available online 15 July 2019

Keywords:
Proto-Tethys Ocean
Magmatic diversity
Slab break-off
West Kunlun Orogen
Tibet
High Sr/Y

ABSTRACT

Continental collision and subsequent slab break-off can induce granitoid magmatism of variable compositions and ages. We present new geochronological and geochemical data from granitoids in the eastern part of the West Kunlun Orogen, situated along the northwestern margin of the Tibetan Plateau. Our data reveal a distinct Late Ordovician–middle Silurian (450–428 Ma) magmatic flare-up event after closure of the Proto-Tethys Ocean (Proto-Kunlun Ocean) and following continental collision. Some high-Sr/Y granitoids show variable whole-rock $(^{87}Sr/^{86}Sr)_i$, $\varepsilon_{Nd}(t)$, $(^{206}Pb/^{204}Pb)_t$, and zircon $\varepsilon_{Hf}(t)$ values, indicating that these rocks were derived from heterogeneous sources comprising both juvenile and older material from the lower crust under amphibolite-facies conditions. We identify a linear spatial distribution of small-scale and short-lived magmatism and magmatic diversity (A-/S-/I-type) along the suture zone, and suggest that this Late Ordovician–middle Silurian magmatism in the West Kunlun Orogen was associated with slab break-off of the Proto-Tethys oceanic plate. The results improve our understanding of the closure of the Proto-Tethys Ocean, crustal growth, and the final formation of Gondwana in the NW Tibetan Plateau region.

© 2019 Elsevier B.V. All rights reserved.

1. Introduction

Collision-related subduction and subsequent slab break-off are expected to occur in a tectonic setting in which closure of an oceanic basin leads to the onset of continental collision and thickening (Davies and von Blanckenburg, 1995). Continental collision slows over time and eventually causes the local subduction process to cease. Subsequently, the occurrence of slab break-off or slab detachment from the lithosphere induces varied post-collisional magmatism, such as that in the Himalayan–Tibetan orogen, the Alps, and the Central Asian Orogenic Belt (Ji et al., 2016; Li et al., 2017a; Mahéo et al., 2002; von Blanckenburg and Davies, 1995; Wang et al., 2016, 2018; Xu et al., 2008; Yin and Harrison, 2000).

The West Kunlun Orogen (WKO) formed during the closure of the Proto-Tethys Ocean along the northwestern margin of the Tibetan Plateau during the Neoproterozoic to early Paleozoic, followed by collision of the Tarim Block to the north and the Gondwana-derived terranes (e.g., Tianshuihai) to the south (Fig. 1A; Yin and Harrison, 2000). This region can therefore improve our understanding of the evolution of the Proto-Tethys Ocean and the final formation of Gondwana (Zhang et al., 2018b, 2018c, 2018d).

The closure time of the Proto-Tethys Ocean and related collision is, however, controversial. Mattern and Schneider (2000) argued using stratigraphic evidence that closure of the Proto-Tethys Ocean started during the Devonian. However, on the basis of a petrological study of high-pressure granulite-facies metamorphic rocks, Wang (2008) proposed that decoupling of the oceanic lithosphere took place during the Ordovician. A similar timing of slab break-off was inferred by Zhou et al. (2000) and Ye et al. (2008) from the age of high Ba–Sr granitoids magmatism, $^{39}Ar/^{40}Ar$ ages from hornblende in the shear zone, and estimates of the conditions of peak metamorphism. In contrast, other researchers have proposed that the high-K granitoids and enclaves were controlled by slab break-off of Proto-Tethys oceanic plate during the middle Silurian (Jia et al., 2013; Liu et al., 2014). However, this age is poorly constrained because high-K calc-alkaline granites can been placed in many different settings (Barbarin, 1999). These uncertainties limit our understanding of the tectonic evolution and crustal formation of the WKO. Moreover, previous studies were confined mainly to the western part of the WKO, so the timing of slab break-off in other places requires further investigation.

Granitoids are the principal component of orogenic crust and are therefore the most characteristic indicator of orogen formation. The compositions of granitoids can retain the geochemical and isotopic signatures of their precursors, commonly recording

* Corresponding author.
E-mail address: zhangqc0721@163.com (Q. Zhang).

https://doi.org/10.1016/j.lithos.2019.07.014
0024-4937/© 2019 Elsevier B.V. All rights reserved.

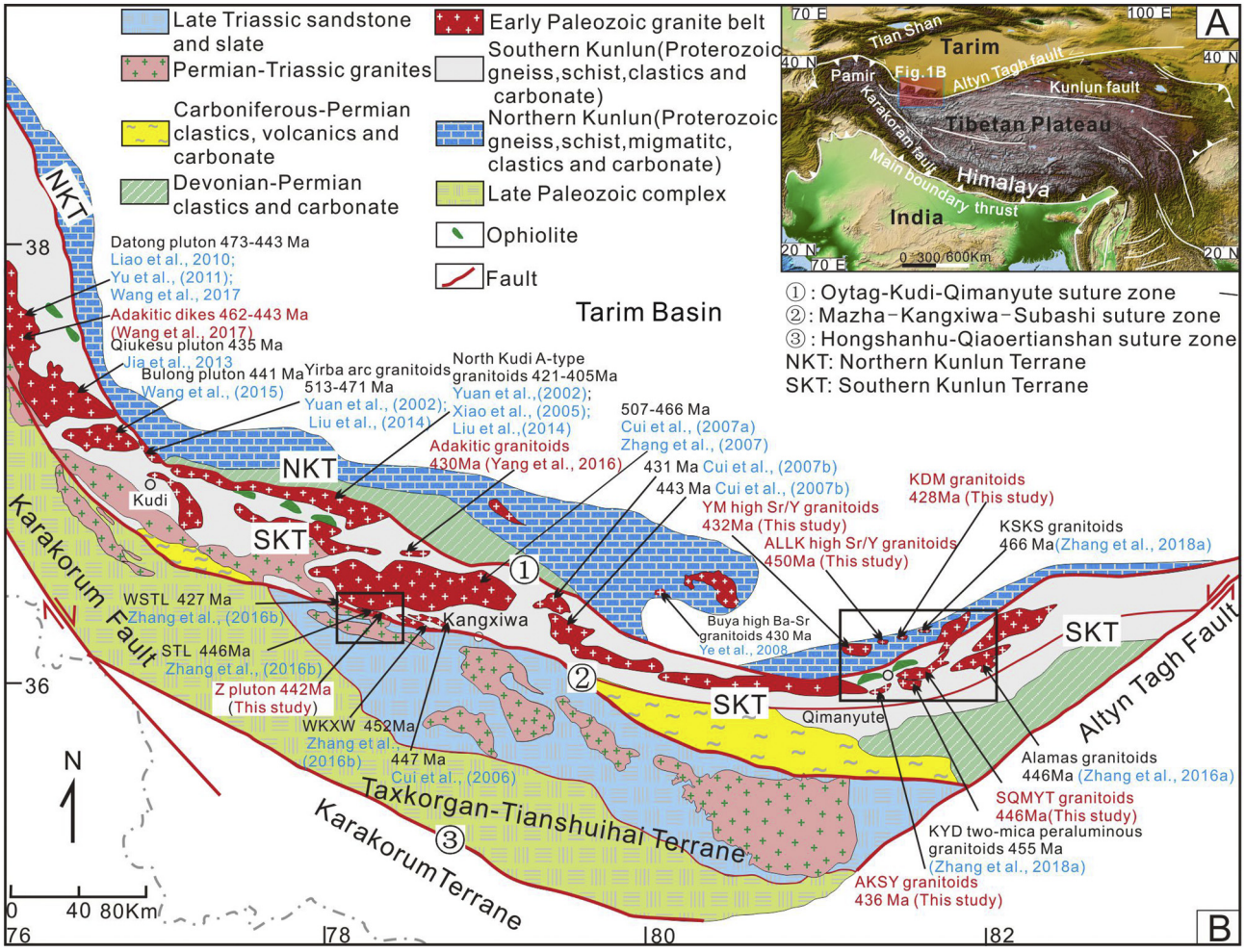

Fig. 1. (A) Simplified geological sketch map of the western Tibetan Plateau, and (B) map of the distribution of early Paleozoic granitoids in the West Kunlun orogenic belt, western China, showing the main geological units discussed in this paper (modified after Yin and Harrison, 2000; Wang, 2004). Ages from previous studies are also shown (all dates are U–Pb zircon ages). ALLK (Alaleike), Z (Xieyila), AKSY (Akesaiyin), SQMYT (South Qimanyute), YM (Yamen), KDM (Kuidaimai) are the six plutons investigated in this study.

contributions from mantle and crustal components in response to distinct tectonic settings. For example, typical adakitic rocks (high-Sr/Y) have been interpreted to be derived from slab melting in response to a subduction-related setting (Defant and Drummond, 1990). Recently, many high-Sr/Y granitoids have been identified as having being emplaced in collision-related settings, and this provides insights into the thermal and physical relationships between syn- to post-orogenic magmatism and tectonic evolution (Chung et al., 2003; Xu et al., 2008; Zeng et al., 2011). Furthermore, continental collision commonly produces linear belts of S-type granites (Yin and Harrison, 2000). Therefore, understanding the magmatic in response to the closure and slab break-off of Proto-Tethys oceanic plate will provide a better understanding of the final orogenic contraction. Thus, knowledge of magma petrogenesis in response to early orogenic evolution in the WKO is essential for understanding the closure of the Proto-Tethys Ocean and the growth of continental crust.

This study reports new geochronological, geochemical, and isotopic data from six early Paleozoic monzonitic–granodioritic–granitic plutons with high-Sr/Y or high-K characteristics in the eastern part of WKO in the context of the evolution of the Proto-Tethys Ocean. By combining our results with other regional magmatic, metamorphic, and lithostratigraphic data, we propose that the identified magmatic "flare-up", the diverse granitoid magmatism, and the growth of continental crust all occurred in response to slab break-off.

2. Geological setting and sample descriptions

2.1. Geological setting

The WKO was formed by multiple terrane-accretion events along the northern margin of the Tibetan Plateau (Fig. 1A; Dewey et al., 1988; Hsü et al., 1995; Yin and Harrison, 2000; Xiao et al., 2002, 2005; Wang, 2004; Jiang et al., 2008, 2013; Zhang et al., 2016a). The WKO can be divided into eastern and western sections. In the present study, the orogen in the western section is tectono-stratigraphically subdivided into four main units: the Northern Kunlun Terrane (NKT; also the Tiekelike belt in the literature; e.g., Pan and Wang, 1994; Zhang et al., 2013; Wang et al., 2013), the narrow Southern Kunlun Terrane (SKT), the Taxkorgan–Tianshuihai Terrane (TSHT), and the Karakorum Terrane (e.g., Pan and Wang, 1994; Zhang et al., 2018b, 2018c; Fig. 1B). In the eastern section, the orogen is also tectono-stratigraphically subdivided into four main units: the NKT (also termed the southern margin of the Tarim Block; e.g., Wang et al., 2003), the narrow SKT, the Taxkorgan–Tianshuihai Terrane, and the Karakorum Terrane, which are separated by different sutures.

The Oytag–Kudi–Qimanyute (OKQ) suture separates the NKT from the SKT. The latter is separated from the Taxkorgan–Tianshuihai Terrane by the Mazha–Kangxiwa–Subashi (MKS) suture zone. The Hongshanhu–Qiaoertianshan (HQ) suture separates the Taxkorgan–Tianshuihai Terrane and the Karakorum Terrane. The ages of these

successive sutures decrease from north to south, that is, from the OKQ to MKS to HQ sutures.

The OKQ suture was first proposed by Pan and Wang (1994) and is generally accepted to be a remnant of the Proto-Tethys Ocean (Jiang et al., 2008; Mattern and Schneider, 2000; Yuan et al., 2002). The OKQ suture zone includes the Oytag plagiogranite, the Kudi ophiolite, and the Qimanyute ophiolite (Han et al., 2002; Jiang et al., 2008; Pan and Wang, 1994; Xiao et al., 2002, 2005; Zhang et al., 2018b, 2018c). The MKS suture zone is composed of the Muztag and Subashi ophiolite sequences (Ji et al., 2004; Jiang et al., 2008, 2013). The HQ suture zone is largely overlain by Cretaceous ophiolite (Liu et al., 2015).

The closure of the Proto-Tethys Ocean (leading to the formation of the OKQ suture) took place either during the Ordovician (e.g., Zhang et al., 2018b, 2018c), the Silurian (e.g., Matte et al., 1996), or the Devonian (e.g., Mattern and Schneider, 2000). The closure age of the Proto-Tethys remains uncertain, largely because of the number of different approaches used by different researchers and the diversity in defining terrane collisions. Hence, more studies are needed to refine the age. There were two periods of Paleo-Tethys oceans: during the first period, an ocean existed between the SKT and the Taxkorgan–Tianshuihai Terrane; and during the second period, an ocean existed between the Taxkorgan–Tianshuihai Terrane and the Karakorum Terrane (Jiang et al., 2013; Liu et al., 2015). Closure of the Paleo-Tethys (leading to the formation of the MKS and HQ sutures) occurred from the late Permian to Late Jurassic (e.g., Mattern and Schneider, 2000; Xiao et al., 2005).

The WKO comprises Precambrian magmatic rocks, Paleozoic magmatic arcs, ophiolitic mélange, accretionary complexes, and arc-related basin sediments (Jiang et al., 2008; Yuan et al., 2002; References therein). Two key magmatic suites have been identified in the SKT, namely, the late Mesoproterozoic–early Paleozoic northern magmatic belt (>1000 km long) and the late Paleozoic–early Mesozoic southern magmatic belt (>1000 km long). The northern magmatic belt along the OKQ suture consists of early Paleozoic arc plutons and ophiolitic mélanges (Xiao et al., 2003). The Cambrian–Ordovician arc magmatism ranges from mafic to felsic in composition and includes gabbros from the NE Pamir (530 Ma), and granitoids from the Yierba pluton (513–471 Ma), from the Kashikashi pluton (466 Ma), and from the Datong pluton (473–448 Ma), which were formed in association with subduction of Proto-Tethys oceanic crust (Liao et al., 2010; Yuan et al., 2002; Zhang et al., 2018a; Zhang et al., 2018b, 2018c). The NKT comprises the Paleoproterozoic Milan and Changchengian Kaqiang groups, and the Sinian–Cambrian Alajiaoyi and Middle Ordovician Pishengaisayi formations, whereas the SKT comprises the Jixiannian Alamas Group, which consists of schist, gneiss, marble, and amphibolite.

2.2. Granitoid geology

Here we describe five granitoid plutons, Alaleike pluton (ALLK), Yamen pluton (YM), Akesaiyin pluton (AKSY), South Qimanyute pluton (SQMYT), and Kuidaimai pluton (KDM). These plutons occur in the Pulu area, in the eastern part of the WKO, and form a NE–SW-trending tectono-magmatic belt that extends for >100 km and exceeds 20 km in width. The exposed area of these granitoid plutons is ca. 600–700 km^2. These rocks are tectonically related to an early Paleozoic ophiolitic mélange belt in the Qimanyute area. The granitoids intrude Mesoproterozoic metamorphic rocks of the Jixianian Alamas, Jixianian Liushui, and Changchengian Kaqiang groups, and the contact between the plutons and wall rocks is steeply sharp. The Xieyila pluton (Z) is located south of the Kudi ophiolitic mélange in the central section of the WKO, and it is intruded into the Changchengian Saitula Group.

The granitoids of the Akesaiyin (AKSY-03), Xieyila (Z-03), and South Qimanyute (SQMYT-03) plutons consist of biotite granites and are typically dominated by medium-grained microcline (20%–35%), plagioclase (30%–40%), quartz (25%–30%), and biotite (5%–10%, Fig. 2). The Kuidaimai granitoids (KDM-03) consist of monzogranites and are typically composed of medium-grained microcline (30%–40%), plagioclase (30%–40%), hornblende (5%–10%), quartz (1%–5%), muscovite (1%–5%), and biotite (1%–5%, Fig. 2). The granitoids of the Alaleike (ALLK-03) and Yamen (YM-03) plutons are mostly granodiorite and are composed of plagioclase (40%–50%), microcline (20%–30%), hornblende (10%–15%), biotite (10%–15%), muscovite (1%–5%), and quartz (20%–25%, Fig. 2). The most abundant accessory minerals in these granitoids are zircon, magnetite, apatite, ilmenite, titanite, and Fe–Ti oxides.

3. Analytical methods

Six samples (ALLK-03, YM-03, Z-03, AKSY-03, SQMYT-03, and KDM-03) were selected for zircon U–Pb dating in this study. We used a Finnigan Neptune inductively coupled plasma–mass spectrometry (ICP–MS) instrument that was connected to a New Wave UP-213laser-ablation (LA) instrument at the Institute of Mineral Resources, Chinese Academy of Geological Sciences (CAGS), Beijing, China. The instrumental protocols and data acquisition methods used followed those of Hou et al. (2009) and Ludwig (2003). Forty-five major-element samples were analyzed using an X-ray fluorescence spectrometer at the National Research Center of Geoanalysis, Chinese Academy of Geological Sciences (CAGS), Beijing, China. The five standard samples (GBW07103, GBW07103, GBW07104, GBW07103, GBW07112) and three replicate samples were analyzed together with the samples, indicating precision and accuracy to within 5 and 10 relative percent for geochemical data. We also analyzed 45 trace-elements sample and 24 Sr–Nd–Pb isotope samples, which were pretreated at Guizhou Tongwei Analytical Technology Co., Ltd. Isotope samples were analyzed using a Thermo Fisher X2 equipped with a CETAC ASX-510auto-sampler, a Nu Plasma HR multi-collector (MC)–ICP–MS instrument with a modified CETAC ASX-110FR auto-sampler, and a DSN-100 dissolution nebulizing system and a DSN-100 dissolution nebulizing system in the Radiogenic Isotope Facility at The University of Queensland (RIF–UQ), Australia. Detailed chemical separation and isotopic measurement procedures followed those of Zhang et al. (2018a). The two standard samples (W-2a, BHVO-2) and one replicate sample (W-2a) were analyzed together with the samples, indicating precision and accuracy to within 5 and 10 relative percent, for geochemical data. Zircon in situ Lu–Hf analyses six granitoid samples were carried out using a NU plasma II MC–ICP–MS instrument at the School of Earth and Space Sciences, Peking University, Peking, China. An ArF excimer LA system (Geolas HD, 193 nm) was used with a 40 μm spot size. The analytical procedure was the same as that described by Zhang et al. (2016b). Data reduction was conducted using the software IOLITE (Paton et al., 2011). To ensure measurement accuracy, zircon Hf isotopes of KDM pluton (samples1e–18e) and YM pluton (samples1e–20e) were analyzed using a Geolas193nm LA microprobe attached to a Neptune MC–ICP–MS instrument at the Institute of Mineral Resources, CAGS, Beijing, China. The instrumental conditions and data acquisition procedures followed those described by Hou et al. (2009). LA spot sizes of 40 μm were applied. The method for Yb and Lu correction followed that of Wu et al. (2006).

4. Results

4.1. Zircon U–Pb geochronology

Zircon grains from the six analyzed granitoid plutons (ALLK-03, YM-03, AKSY-03, Z-03, SQMYT-03, and KDM-03) range in size from 50 to 200 μm and have length-to-width ratios of 1:1 to 3:1. The grains are predominantly euhedral tabular crystals, prismatic, and colorless, with oscillatory zoning (Fig. 3). In each case, we assumed that the weighted mean $^{206}Pb/^{238}U$ age represents the emplacement age of the granitoid.

Forty spots were analyzed for sample SQMYT-03, yielding $^{206}Pb/^{238}U$ ages ranging from 447 to 431 Ma. These ages are mostly concordant and define a weighted mean $^{206}Pb/^{238}U$ age of 438 ± 2 Ma (1σ, MSWD = 0.36). The 35 spots for ALLK granodiorite yielded concordant $^{206}Pb/^{238}U$ ages of 458–443 Ma and define a weighted mean

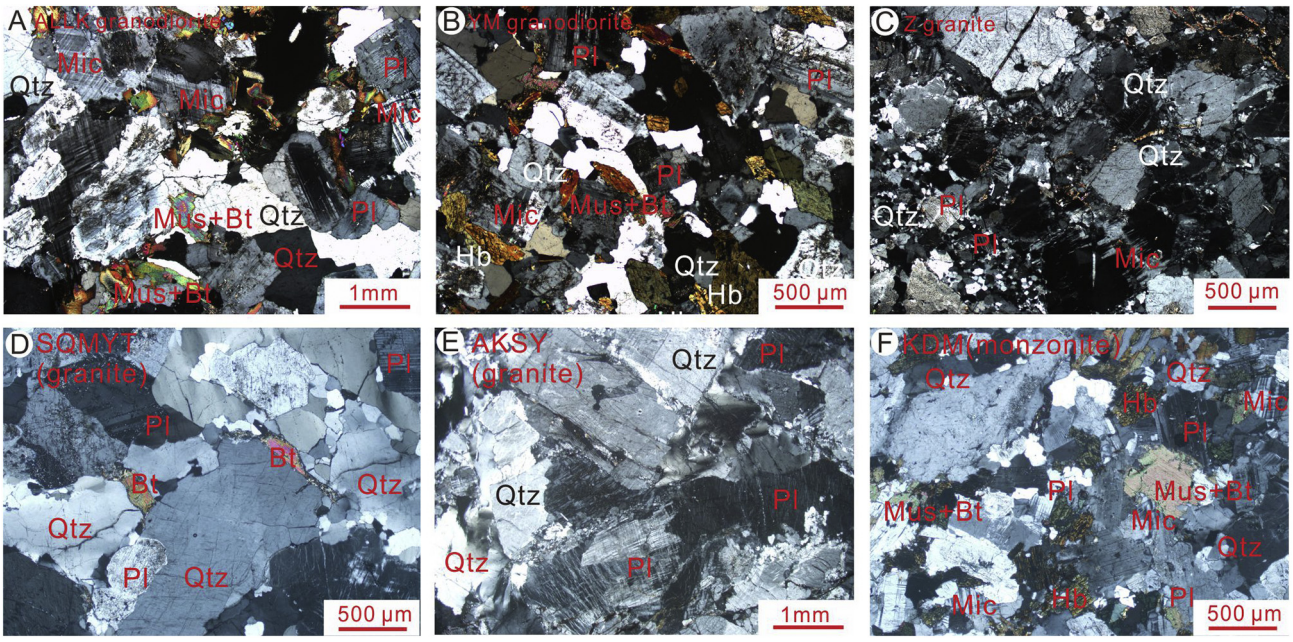

Fig. 2. Photomicrographs of high-Sr/Y and high-K intrusions in the West Kunlun Orogenic Belt. (A) ALLK granodiorite (high Sr/Y) from the Alaleike pluton; (B) YM granodiorite (high-Sr/Y) from the Yamen pluton; (C) Zgranite (high-K) from the Xieyila pluton; (D) SQMYT granite from the South Qimanyute pluton; (E) AKSY granite from the Akesaiyin pluton; (F) KDM monzonite from the Kuidaimai pluton. Hb, hornblende; Bt, biotite; Mus, muscovite; Mic, microcline; Pl, plagioclase; Qt, quartz.

$^{206}Pb/^{238}U$ age of 450 ± 2 Ma (MSWD = 0.46). The 35 spots for YM granodiorite are concordant to near concordant and yield $^{206}Pb/^{238}U$ ages of 441–425 Ma and define a weighted mean $^{206}Pb/^{238}U$ age of 432 ± 2 Ma (MSWD = 0.61). The younger $^{206}Pb/^{238}U$ age of 422 ± 10 (YM-03-08) is discordant owing to the loss of radioactive Pb. The 10 spots of Z-03 sample yielded $^{206}Pb/^{238}U$ ages ranging from 450 to 437 Ma. These ages are concordant and define a weighted mean $^{206}Pb/^{238}U$ age of 442 ± 3 Ma (MSWD = 0.80). The 23 spots analyzed for KDM-03 yielded $^{206}Pb/^{238}U$ ages ranging from 436 to 420 Ma. These ages are mostly concordant and define a weighted mean $^{206}Pb/^{238}U$ age of 428 ± 3 Ma (MSWD = 0.49). Thirty-four spots for AKSY-03 were analyzed, and they yielded $^{206}Pb/^{238}U$ ages ranging from 445 to 431 Ma. These mostly concordant 34 analyses define a weighted mean $^{206}Pb/^{238}U$ age of 436 ± 2 Ma (MSWD = 0.35).

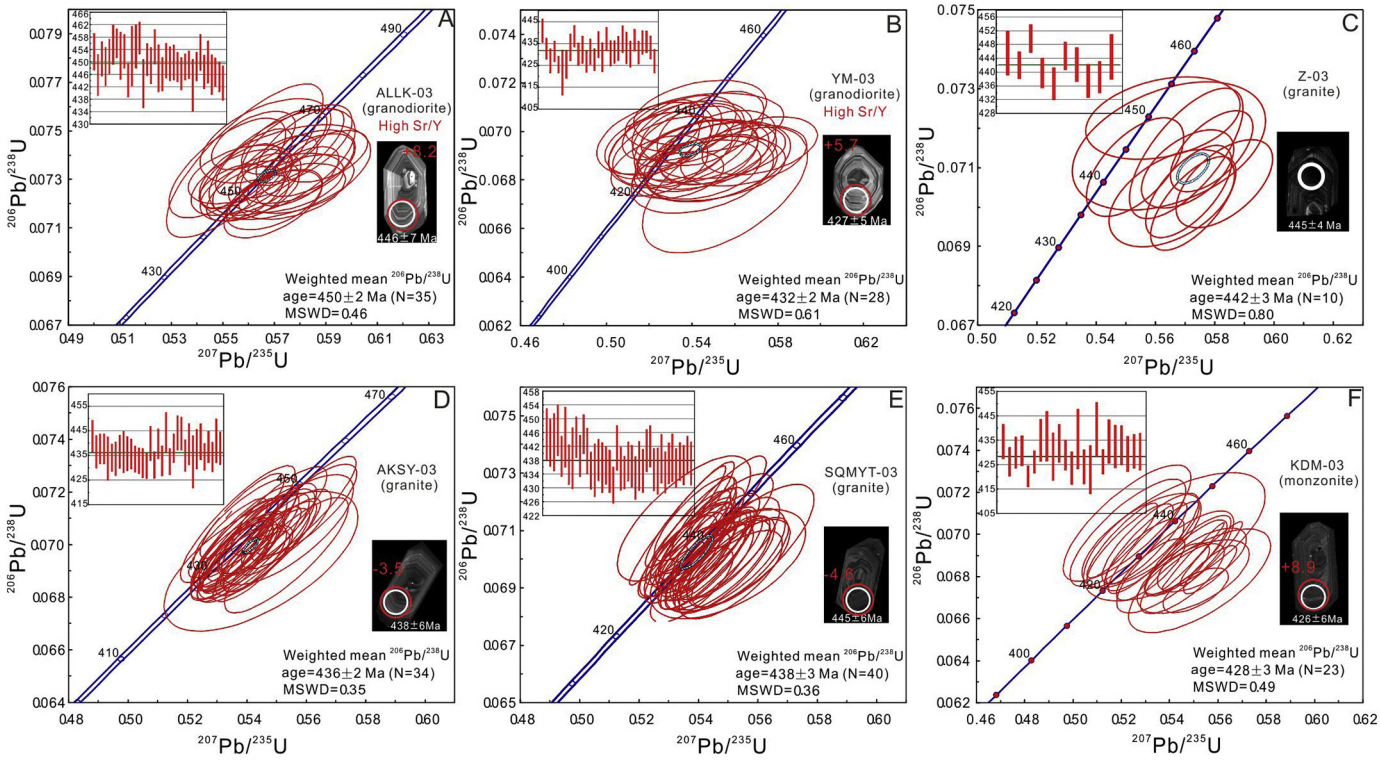

Fig. 3. U–Pb concordia diagrams showing zircon ages obtained by LA–ICP–MS. (A) Sample ALLK-03, (B) sample YM-03, (C) sample Z-03, (D) sample AKSY-03, (E) sample SQMYT-03, (F) sample KDM-03. Zircon U–Pb ages (white circles) and $\varepsilon_{Hf}(t)$ values (red circles).

4.2. Whole-rock major- and trace-element geochemistry

The Late Ordovician–middle Silurian granitoids can bedivided into two groups: high-Sr/Y granitoids and high-K granitoids. The high-Sr/Y granitoids from the two plutons of ALLK and YM show variation in SiO_2 (64.5–72.1 wt.%), K_2O (1.12–2.02 wt.%), Na_2O (3.82–5.03 wt.%), and CaO (2.23–4.96 wt.%) contents (Table 1 and Supplement table S2), and record granodiorite–granite compositions with calcic to calc-alkalic characteristics (Fig. 4A and B). These granitoids have uniform contents of MgO and FeO (Table 1 and Supplement table S2) and are metaluminous to weakly peraluminous (Fig. S1). All samples show high Al_2O_3 contents (>14 wt.%) and high Na_2O/K_2O ratios (>2.0). These granitoids have mostly high La/Yb (>12, Table 1 and Supplement table S2) and Sr/Y (>45, Fig. 4C) ratios but variable Cr and MgO contents, which distinguishes them from the early–middle Ordovician granitoids (Fig. 4C).

The high-Sr/Y granitoids can be divided into two groups: (1) ALLK high-Sr/Y granitoids with low Cr, MgO, and Sr contents (Table 1); and (2) YM high-Sr/Y granitoids with high Cr, MgO, and Sr contents (Supplement table S2). The ALLK granitoids record low Sr contents with elevated K/Na ratios, a result of the relative abundance of residual plagioclase in the source. All samples are depleted in Nb, Ta, Ti, and P, although they are enriched in LILEs (large ion lithophile elements) and show enrichment in LREEs (light rare earth elements) (mostly $(La/Yb)_N > 7.7$), and low and nearly flat HREE (heavy rare earth elements) ($(Gd/Yb)_N$=1.5–3.1) patterns. (See Table 1 and Supplement table S2.)

The ALLK granitoids have weak negative to positive Eu anomalies with $Eu/Eu^* = 0.9–2.1$, whereas the YM granitoids have weak negative anomalies with $Eu/Eu^* = 0.9–1.0$ (Fig. 5). Notably, the YM high-Sr granitoids have higher total REE contents compared with the ALLK low-Sr granitoids. The granitoids show compositional similarities to coeval high Ba–Sr granitoids in the WKO (Figs.1 and 5), high-SiO_2 adakites (Martin et al., 2005), the Cordillera Blanca Na-rich batholith (Petford and Atherton, 1996), and southern Tibet collision-type adakites (Fig. 5; Chung et al., 2003).

The early–middle Silurian high-K granitoids have high SiO_2 (60.3–76.6 wt.%) and K_2O (3.74–6.26 wt.%) contents, moderate Na_2O content (2.34–4.49 wt.%) and low Fe_2O_3 (0.04–2.23 wt.%), MgO (0.08–1.01% wt.%), mostly Mg# (11–36) and CaO (0.79–2.63 wt.%) contents (Supplement table S2). They exhibit mostly high-K calc-alkaline and shoshonitic characteristics (Fig. 4B) and are metaluminous to weakly peraluminous (Fig. S1). On a chondrite-normalized REE diagram, these granitoids have weak to moderate fractionated REE

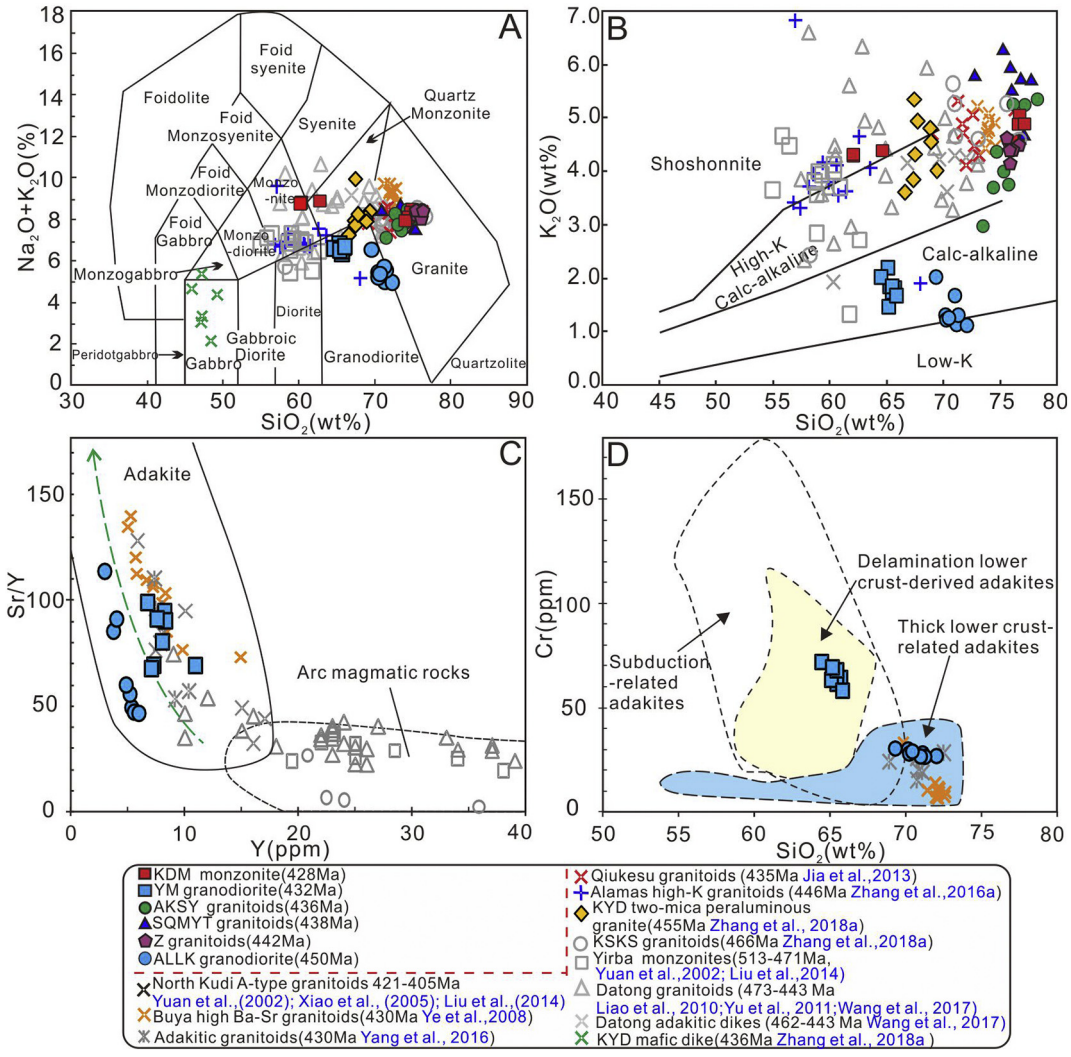

Fig. 4. (A) $K_2O + Na_2O$ vs. SiO_2 classification diagram (after Middlemost, 1994); (B) K_2O vs. SiO_2 classification diagram (after Peccerillo and Taylor, 1976) for early Paleozoic granitoids in the West Kunlun orogenic belt, western China. (C) Sr/Y vs. Y diagram for early Paleozoic high-Sr/Y granitoids from the ALLK and YM plutons, indicating the high-Sr/Y characteristics distinct from early–middle Ordovician granitoids in the area. Fields of adakite and typical arc magmatic rocks are after Richards and Kerrich (2007). (D) Cr vs. SiO_2 diagram for late Ordovician–early Silurian granitoids, indicating characteristics of adakites derived from thickened lower crust. Fields of subduction-related adakites, delamination-related adakites, thickened lower crust-derived adakites, metabasaltic and eclogite experimental melts hybridized with peridotite, and metabasaltic and eclogite experimental melts (1–4 GPa) are after Wang et al. (2006).

Table 1
Chemical compositions of the high Sr/Y granitoids at the northwestern Tibetan Plateau.

Pluton	ALLK pluton-high Sr/Y							
Sample	ALLK-01	ALLK-02	ALLK-03	ALLK-04	ALLK-05	ALLK-06	ALLK-07	ALLK-08
Major elements (wt.%)								
SiO_2	71.16	72.08	70.2	71.32	70.28	71.03	69.35	70.48
Al_2O_3	15.15	14.98	14.93	15.08	14.75	14.89	15.39	14.95
CaO	3.77	3.76	3.61	3.38	3.44	3.33	2.93	3.24
Fe_2O_3	1.01	0.84	1.02	0.78	1.05	0.78	1.02	1.05
FeO	1.42	1.56	1.49	1.56	1.49	1.56	1.56	1.63
K_2O	1.14	1.12	1.32	1.32	1.22	1.68	2.02	1.26
MgO	1.23	1.21	1.19	1.16	1.28	1.16	1.25	1.36
MnO	0.04	0.04	0.04	0.04	0.04	0.04	0.04	0.05
Na_2O	3.83	3.82	4.09	4.21	3.98	4.03	4.51	4.1
P_2O_5	0.05	0.05	0.09	0.09	0.09	0.08	0.09	0.09
TiO_2	0.3	0.29	0.3	0.29	0.3	0.28	0.3	0.32
LOI	0.84	0.62	1.15	0.95	1.14	0.75	1.45	1.3
Total	99.94	100.37	99.43	100.18	99.06	99.61	99.91	99.83
Mg#	0.49	0.48	0.47	0.48	0.49	0.48	0.48	0.49
Tarce elements (ppm)								
Li	18.6	16.9	18	17.4	18.3	16.3	14	17.4
Sc	3.55	3.68	3.84	3.78	4.08	3.54	3.39	4.11
Ti	1560	1510	1600	1510	1600	1520	1580	1700
V	35.2	34.3	32.6	30.4	32.4	31	37.2	35.4
Cr	28.2	26.9	30.1	26.5	28.1	26.7	30.5	29.1
Mn	314	302	311	300	323	307	289	356
Co	6.12	5.9	6.24	5.85	6.42	5.84	6.38	6.87
Ni	15	14.6	15.3	14.4	15.5	14.4	15.2	16.4
Cu	12.1	7.76	13.6	13	15.1	15.9	10.5	12.4
Zn	38.7	34	43	41.2	44.8	42.5	42.1	50.4
Ga	15.2	14.8	15.1	15.2	15.1	15.2	15.3	15.6
Rb	28.5	22.3	20.7	29.5	27.4	39.5	62.7	34.5
Sr	334	317	263	288	290	262	364	278
Y	2.93	3.7	5.3	5.15	4.81	5.52	3.98	5.93
Zr	130	134	114	127	122	109	112	129
Nb	5.28	4.68	6.61	6.12	6.61	6.8	7.23	7.35
Sn	0.613	0.569	0.595	0.559	0.58	0.618	0.53	0.685
Cs	1.74	1.83	0.561	1.19	0.715	1.79	0.848	0.899
Ba	376	351	533	543	538	675	809	645
La	6.12	6.99	13.4	16.3	9.14	14.1	11.2	15.6
Ce	9.13	11.3	22.9	27.7	15.6	20.6	18.4	25.7
Pr	0.978	1.22	2.43	2.91	1.75	2.56	1.99	2.88
Nd	3.42	4.39	8.55	9.96	6.31	8.9	6.95	10.1
Sm	0.612	0.817	1.51	1.65	1.18	1.54	1.16	1.76
Eu	0.402	0.415	0.458	0.463	0.446	0.446	0.464	0.47
Gd	0.545	0.722	1.25	1.29	1	1.24	0.979	1.44
Tb	0.0835	0.111	0.176	0.178	0.149	0.183	0.137	0.205
Dy	0.477	0.638	0.938	0.939	0.827	0.974	0.734	1.08
Ho	0.0963	0.128	0.181	0.173	0.163	0.187	0.137	0.201
Er	0.277	0.36	0.488	0.467	0.454	0.51	0.356	0.535
Tm	0.0439	0.0577	0.0742	0.0724	0.0715	0.0789	0.0508	0.0814
Yb	0.306	0.388	0.482	0.47	0.482	0.522	0.322	0.518
Lu	0.0506	0.0632	0.0766	0.0734	0.0767	0.0805	0.0495	0.0819
Hf	2.99	3.21	2.85	3.08	3.04	2.69	2.64	3.13
Ta	0.444	0.438	0.602	0.538	0.581	0.669	0.46	0.609
Pb	11.7	10.1	12.6	13	12	13.8	6.49	15.4
Th	2.44	2.73	5.08	5.89	3.73	5.53	3.24	6.24
U	0.552	0.681	0.801	0.804	0.747	0.724	0.556	0.981
$(La/Yb)_N$	14.3	12.9	19.9	24.9	13.6	19.4	24.9	21.6
Eu/*Eu	2.1	1.6	1.0	0.9	1.2	1.0	1.3	0.9
T_{Zr}	767	770	751	764	760	750	750	767

Note: T_{Zr}=12,900/(2.95+0.85M+ln$D^{Zr,\ zircon/melt}$) (Watson and Harrison, 1983), where $D^{Zr,\ zircon/melt}$ is the ratio of Zr concentrations (ppm) in zircon to that in the saturated melt, M= cation ratio (Na+K+2·Ca)/(Al · Si).Mg#=M(Mg^{2+})/(M(Mg^{2+}) + M(Fe^{2+})), (M is the molar proportions), ^{T}FeO=0.8998*Fe_2O_3 + FeO. $(La/Yb)_N$, Normalization values are from Sun and McDonough (1989).

patterns, with $(La/Yb)_N$ ranging from 1.5 to 22.3 and low total REE (ΣREE) contents (21.5–333.4 ppm) (Fig. 4E). A flat HREE pattern shows low values with $(Gd/Yb)_N$ ranging from 0.5 to 2.1.

The rocks of AKSYand KDM plutons have moderate negative Eu anomalies. The rocks of SQMYT and Z plutons show strong negative Eu anomalies, except for samples SQMYT-02, 03, 07, and 08, which show weak negative to positive Eu anomalies (Supplement table S2). On a primitive-mantle-normalized spider diagram (Fig. 5E, F), these granitoids are all relatively depleted in high-field-strength elements (HFSEs, such as Ta, Nb, P, and Ti) and have relatively high Rb, Th, and U contents and low Ba and Sr contents (Supplement table S2).

4.3. Whole-rock Sr–Nd–Pb isotopes and zircon Hf isotopes

Whole-rock Sr–Nd–Pb isotopic compositions (24 samples), zircon Hf isotopes for six granitoid plutons (ALLK,YM, Z, AKSY, SQMYT, and KDM), and Pb isotope data for the Kayedi S-type granitoids are given in supplement (Tables 2 and 3) and plotted in Fig. 6. Their initial $(^{87}Sr/^{86}Sr)_t$, $\varepsilon_{Nd}(t)$, $Pb_{(t)}$, and $\varepsilon_{Hf}(t)$ values

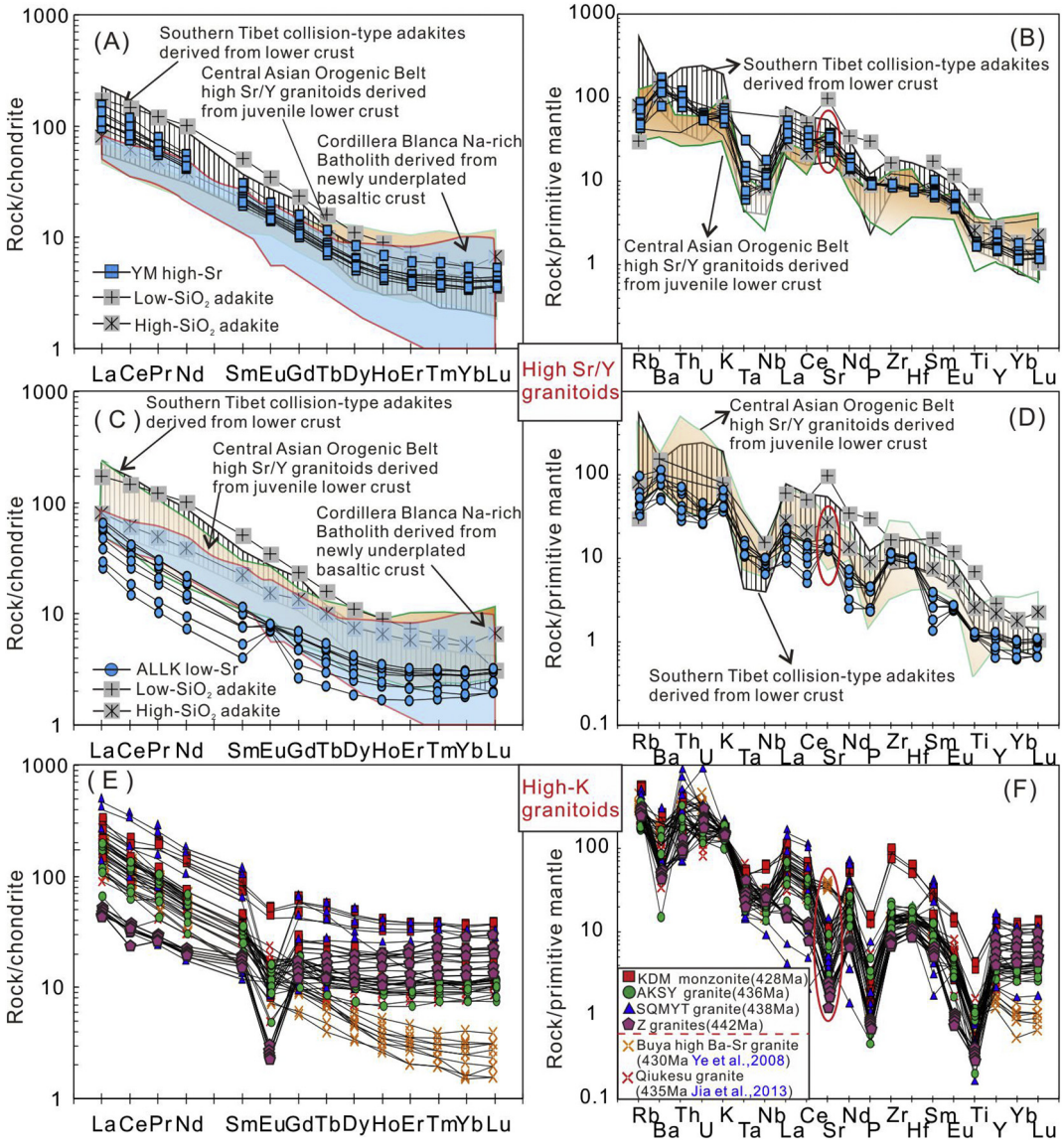

Fig. 5. (A and C) Chondrite-normalized rare earth element patterns, and (B and D) primitive-mantle-normalized trace-element spider diagrams for the high-Sr/Y granitoids (ALLK and YM) in the West Kunlun orogenic belt. (E) Chondrite-normalized rare earth element patterns, and (F) primitive mantle normalized trace element spider diagrams for the high-K granitoids (Z, AKSY, AQMYT, and KDM) in the West Kunlun orogenic belt. The values for chondrite and primitive-mantle normalization are from Sun and McDonough (1989). Shaded fields with vertical lines are southern Tibet collision-type lower-crust-derived adakites, Central Asian Orogenic Belt high-Sr/Y granitoids derived from juvenile lower crust, and Cordillera Blanca Na-rich batholith from newly underplated basaltic crust, after Chung et al. (2003), Petford and Atherton (1996), and Li et al. (2017a). The average values for low-SiO_2 adakite and high-SiO_2 adakite are from Martin et al. (2005). Symbols are as in Fig. 3.

were calculated using the ages determined by LA–ICP–MS zircon U–Pb analysis. The Rb–Sr isotope system is sometimes susceptible to post-magmatic perturbations, which causes many older granitoid rocks to yield unrealistic initial Sr isotope compositions. Unfortunately, the initial $^{87}Sr/^{86}Sr$ (I_{Sr}) values of eight samples (KDM and Z plutons) show this feature, with $^{87}Sr/^{86}Sr$ (I_{Sr}) values of < 0.7000. The remaining 16 samples (ALLK, YM, AKSY, and SQMYT) yield $(^{87}Sr/^{86}Sr)_t$ = 0.7055–0.7104.

The 16 samples of high-K granitoids (Z, AKSY, SQMYT, and KDM) yield $\varepsilon_{Nd}(t)$ values of −7.7 to −2.1, and two-stage Nd model ages (T_{DM2}) of 2.01–1.41 Ga. The two high-K granitoids (AKSY and SQMYT) have similar Hf compositions with predominantly negative $\varepsilon_{Hf}(t)$ values (−7.0 to −0.5) and two-stage Hf model ages (T_{DM2}) of 1.85–1.45 Ga. The high-K granitoids show similar behavior of their Lu–Hf and Sm–Nd systems during magmatism, indicating contributions from mature continental crust. The KDM granitoids, however, have positive $\varepsilon_{Hf}(t)$ values of 0.1 to 11.9 and a wider range of two-stage Hf model ages (T_{DM2}) of 1.40–0.66 Ga. These data indicate a significant contribution from juvenile mafic material, which is inconsistent with the negative $\varepsilon_{Nd}(t)$ values in the other high-K granitoids. The high Sr/Y YM granitoids yield $\varepsilon_{Nd}(t)$ values of –2.4 to –2.3 with two-stage Nd model ages (T_{DM2}) of 1.41-1.43 Ga, but yield positive $\varepsilon_{Hf}(t)$ values (+1.2 to +7.2) with relatively young two-stage Hf model ages (T_{DM2}= 0.96-1.34 Ga). These granitoids also show decoupled Nd–Hf values, which is consistent with the high-K granitoids (KDM). However, the high-Sr/Y ALLK granitoids yield positive $\varepsilon_{Nd}(t)$ values of 0.8 to 1.4 with relatively young two-stage Nd model ages (T_{DM2}) of 1.18–1.12 Ga, and $\varepsilon_{Hf}(t)$ values (+7.2 to +12.1) giving young two-stage Hf model ages (T_{DM2}=0.97–0.66 Ga), also suggesting juvenile crustal contributions.

5. Discussion

5.1. Four major tectonic–magmatic episodes along the OKQ suture zone

Four major tectonic–magmatic episodes have been identified along the OKQ suture zone in response to progressive closure of the

Table 2
Sr-Nd isotopic data of the high Sr/Y and high-K granitids at the northwestern Tibetan Plateau.

Sample	Pluton	Rb (ppm)	Sr (ppm)	$^{87}Rb/^{86}Sr$	$^{87}Sr/^{86}Sr$	σm	Sr_i	Sm (ppm)	Nd (ppm)	$^{147}Sm/^{144}Nd$	$^{143}Nd/^{144}Nd$	2σm	$f_{Sm/Nd}$	$\varepsilon_{Nd}(t)$	T_{DM} (Ga)	T_{DM2} (Ga)
ALLK-01	High Sr/Y	29	334	0.25	0.707123	9	0.7055	0.6	3.4	0.1089	0.512430	6	-0.49	1.0	1.05	1.16
ALLK-02		22	317	0.20	0.706990	9	0.7057	0.8	4.4	0.1133	0.512435	5	-0.47	0.8	1.09	1.18
ALLK-03		21	263	0.23	0.707613	9	0.7062	1.5	8.6	0.1075	0.512430	5	-0.50	1.1	1.04	1.15
ALLK-04		30	288	0.30	0.707503	10	0.7056	1.7	10.0	0.1008	0.512424	5	-0.53	1.3	0.98	1.12
YM-01		45	645	0.20	0.707347	8	0.7061	3.5	22.3	0.0944	0.512226	5	-0.56	-2.4	1.18	1.43
YM-02		48	665	0.21	0.707434	8	0.7061	2.9	19.0	0.0923	0.512223	6	-0.57	-2.3	1.16	1.42
YM-03		44	779	0.16	0.706974	8	0.7060	3.8	25.6	0.0911	0.512223	7	-0.57	-2.3	1.15	1.41
YM-04		55	757	0.21	0.707296	10	0.7060	4.6	25.1	0.1106	0.512273	5	-0.48	-2.4	1.30	1.44
SQMYT-01	High-K	235	79	8.61	0.759693	15	0.7060	9.1	47.7	0.1164	0.512044	5	-0.45	-7.1	1.73	1.88
SQMYT-02		234	100	6.82	0.750299	9	0.7078	0.8	1.9	0.2482	0.512393	6	0.16	-7.7	——	——
SQMYT-03		215	304	2.05	0.723137	10	0.7104	1.4	4.7	0.1778	0.512249	5	-0.17	-6.5	——	——
SQMYT-04		293	102	8.35	0.759704	10	0.7076	16.1	83.4	0.1175	0.512059	5	-0.45	-6.9	1.73	1.86
AKSY-01		123	184	1.94	0.719670	11	0.7076	4.1	24.7	0.1020	0.512261	5	-0.52	-2.1	1.21	1.41
AKSY-02		109	125	2.53	0.722517	9	0.7068	3.6	19.6	0.1102	0.512268	5	-0.48	-2.4	1.30	1.45
AKSY-03		106	143	2.15	0.722629	7	0.7093	4.6	26.8	0.1038	0.512263	4	-0.51	-2.1	1.23	1.42
AKSY-04		111	141	2.28	0.721729	7	0.7076	4.9	29.5	0.1011	0.512233	5	-0.53	-2.6	1.24	1.45
Z-01		197	43	13.44	0.781326	9	0.6967	2.9	10.1	0.1748	0.512305	4	-0.18	-5.3	——	2.01
Z-02		186	38	14.10	0.775227	10	0.6864	2.5	10.1	0.1507	0.512237	4	-0.29	-5.2	2.20	1.82
Z-03		198	36	16.11	0.777679	10	0.6763	2.5	9.4	0.1606	0.512277	4	-0.25	-5.0	2.50	1.86
Z-04		192	26	21.52	0.783751	9	0.6482	2.3	9.5	0.1486	0.512241	4	-0.30	-5.0	2.10	1.79
KDM-01		277	61	13.34	0.780933	10	0.6996	5.9	30.9	0.1162	0.512211	5	-0.46	-3.9	1.49	1.59
KDM-02		311	52	17.45	0.792712	11	0.6864	5.3	27.1	0.1193	0.512213	4	-0.44	-4.1	1.51	1.60
KDM-03		307	56	16.10	0.785803	10	0.6877	5.1	27.0	0.1154	0.512203	5	-0.46	-4.0	1.47	1.60
KDM-04		274	48	16.68	0.788888	9	0.6872	4.8	24.2	0.1195	0.512215	5	-0.44	-4.0	1.51	1.60
W-2a	Standard sample				0.707006	8					0.512535	5				
BHVO-2					0.703507	9					0.512988	5				

Note: $\varepsilon_{Nd} = (((^{143}Nd/^{144}Nd)_s / (^{143}Nd/^{144}Nd)_{CHUR} - 1) \times 10000$, $f_{Sm/Nd} = (^{147}Sm/^{144}Nd)_s / (^{147}Sm/^{144}Nd)_{CHUR} - 1$, where s = sample, $(^{143}Nd/^{144}Nd)_{CHUR} = 0.512638$, and $(^{147}Sm/^{144}Nd)_{CHUR} = 0.1967$. The model ages ($T_{DM}$) were calculated using a linear isotopic ratio growth equation: $T_{DM} = 1/\lambda \times \ln(1 + ((^{143}Nd/^{144}Nd)s - 0.51315)/((^{147}Sm/^{144}Nd)_s - 0.2137))$.

Proto-Tethys Ocean and final amalgamation of the WKO (Jiang et al., 2008; Xiao et al., 2002, 2005; Zhang et al., 2018b, 2018c, 2018d): (1) the Cambrian–Middle Ordovician (530–466 Ma), with bi-directional subduction (dominantly southward subduction), development of the back-arc basin, Proto-Tethys oceanic slab subduction and rollback, and emplacement of the OKQ ophiolites, which were formed in a forearc or island arc setting (Fang et al., 2003; Jiang et al., 2008; Yang et al., 1996; Yuan et al., 2005); (2) the late Middle

Table 3
Pb isotopic data of the high Sr/Y and high-K granitids at the northwestern Tibetan Plateau.

Sample	Pluton	Pb/ppm	Th/ppm	U/ppm	$^{208}Pb/^{204}Pb$	$^{207}Pb/^{204}Pb$	$^{206}Pb/^{204}Pb$	$(^{208}Pb/^{204}Pb)_t$	$(^{207}Pb/^{204}Pb)_t$	$(^{206}Pb/^{204}Pb)_t$
ALLK-01	High Sr/Y	11.7	2.4	0.6	38.300	15.629	18.376	37.956	15.615	18.127
ALLK-02		10.1	2.7	0.7	38.353	15.641	18.547	37.906	15.621	18.191
ALLK-03		12.6	5.1	0.8	38.593	15.645	18.573	37.923	15.626	18.236
ALLK-04		13.0	5.9	0.8	38.643	15.640	18.532	37.890	15.622	18.205
YM-01		12.3	8.5	1.4	38.868	15.656	18.543	37.766	15.625	17.984
YM-02		11.3	7.1	1.1	38.794	15.652	18.466	37.794	15.625	17.967
YM-03		22.9	10.2	1.1	38.613	15.628	18.200	37.906	15.614	17.951
YM-04		18.5	7.3	1.3	38.598	15.637	18.261	37.969	15.618	17.914
KYD-01	Two-mica peraluminous	19.8	21.2	4.3	39.821	15.698	19.689	37.963	15.631	18.491
KYD-02		16.3	21.2	5.2	39.851	15.732	20.237	37.577	15.632	18.454
KYD-03		8.0	27.9	3.3	40.802	15.770	20.967	34.543	15.638	18.620
KYD-04		10.5	24.6	4.5	40.603	15.800	21.610	36.388	15.662	19.151
SQMYT-01	High-K	47.5	48.3	7.6	39.741	15.710	19.728	38.044	15.663	18.883
SQMYT-02		44.2	40.9	20.7	38.876	15.807	21.429	37.313	15.667	18.909
SQMYT-03		29.5	6.8	3.3	38.621	15.671	19.040	38.246	15.638	18.454
SQMYT-04		40.5	92.0	6.2	41.552	15.733	20.126	37.650	15.687	19.289
AKSY-01		20.6	29.6	2.7	39.953	15.693	19.674	37.561	15.655	18.992
AKSY-02		15.7	15.1	3.0	39.318	15.671	19.349	37.738	15.616	18.359
AKSY-03		17.4	17.8	3.3	39.423	15.668	19.398	37.739	15.613	18.404
AKSY-04		15.7	16.2	2.78	39.478	15.665	19.284	37.781	15.614	18.356
Z-01		25.7	11.3	4.9	38.784	15.702	19.478	38.055	15.646	18.473
Z-02		23.7	8.5	6.3	38.796	15.703	19.484	38.200	15.625	18.080
Z-03		21.3	7.4	4.5	38.932	15.730	19.962	38.348	15.667	18.836
Z-04		19.7	7.3	4.7	38.861	15.711	19.613	38.245	15.640	18.346
KDM-01		37.4	30.8	6.1	39.393	15.688	19.403	38.062	15.642	18.570
KDM-02		32.2	31.6	5.8	39.295	15.704	19.671	37.706	15.652	18.744
KDM-03		35.1	30.7	6.0	39.334	15.703	19.641	37.918	15.654	18.757
KDM-04		37.2	36.4	6.2	39.327	15.706	19.740	37.740	15.658	18.874
W-2a	Standard sample				38.615	15.659	18.745			
BHVO-2					38.292	15.562	18.592			

Note: Initial Pb isotope ratios were calculated by LA-ICP-MS zircon U-Pb data. $(^{208}Pb/^{204}Pb)_i = (^{208}Pb/^{204}Pb)_{measured} - \mu/(e^{\lambda t} - 1)$, $(^{207}Pb/^{204}Pb)_i = (^{207}Pb/^{204}Pb)_{measured} - \mu/137.88(e^{\lambda t} - 1)$, $(^{206}Pb/^{204}Pb)_i = (206Pb/204Pb)_{measured} - \omega(e^{\lambda t} - 1)$, $\lambda^{238}U = 1.55125 * 10^{-10}/a$, $\lambda^{235}U = 9.8485 * 10^{-10}/a$, $\lambda^{232}Th = 4.9475 * 10^{-11}/a$.

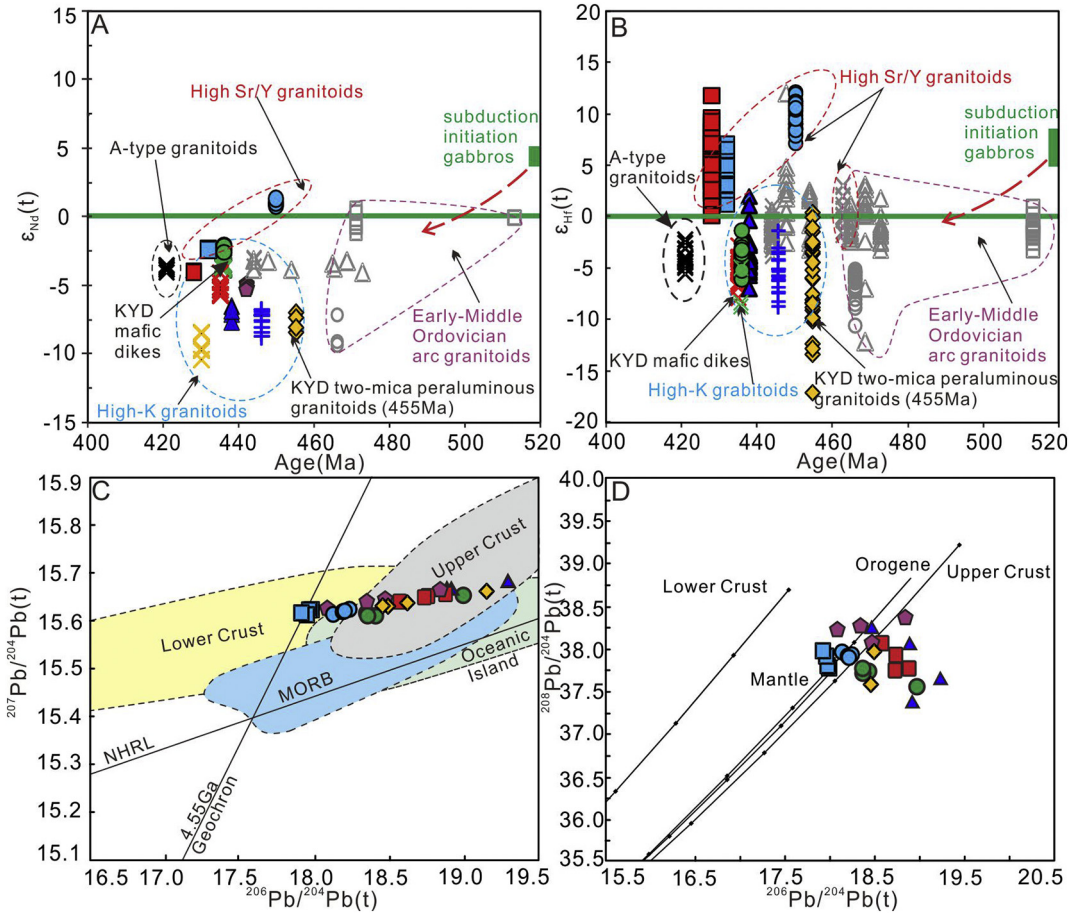

Fig. 6. (A) $\varepsilon_{Nd}(t)$ vs. U–Pb age, (B) $\varepsilon_{Hf}(t)$ vs. U–Pb age, (C) $^{207}Pb/^{204}Pb$ vs. $^{206}Pb/^{204}Pb$, and (D) $^{208}Pb/^{204}Pb$ vs. $^{206}Pb/^{204}Pb$ (after Zartman and Doe, 1981) diagrams for high-Sr/Y and high-K granitoids in the West Kunlun orogenic belt. The values from subduction-initiation gabbros are from Zhang et al. (2018b). Symbols are as in Fig. 3.

Ordovician–middle Late Ordovician (460–450 Ma), with initial collision between the SKT and the NKT, termination of marine sedimentation, and minor syn-collisional peraluminous magmatism (Ye et al., 2008; Zhang et al., 2018a); (3) the middle Late Ordovician–late Silurian (450–428 Ma), which was the collisional orogenic stage with linear magmatism, slab break-off, and high-pressure granulite-facies metamorphism (Yuan et al., 2002; Wang, 2008); and (4) the late Silurian–early Devonian (428–400 Ma), which was the post-orogenic stage with emplacement of A-type granitoids, highly evolved granitoids, and coeval lamprophyre dikes (Yuan et al., 2002).

During the Cambrian–Middle Ordovician (530–466 Ma, the first episode), tectonic activity continued with subduction and arc formation along the OKQ suture zone (e.g., Liao et al., 2010; Yuan et al., 2002; Zhang et al., 2018a). The latest Middle Ordovician (~466 Ma) magmatism occurred as a response to the last magmatic episode of a prolonged magmatic flare-up, which occurred from the Cambrian to Middle Ordovician (Zhang et al., 2018a). Subsequently, final amalgamation and initial collision (460–450 Ma, the second episode) of the NKT (Tarim Block) and SKT resulted in the cessation of arc magmatism, accompanied by a short magmatic quiescent period in the WKO and the disappearance of marine strata (Yuan et al., 2002). Meanwhile, at ~455 Ma, syn-collisional peraluminous magmatism occurred, derived from a metasedimentary-dominated source with minor mantle materials within the middle–upper crust (Zhang et al., 2018a). During this time, there was no large-scale continental shortening or thickening, and minor high-pressure, high-temperature metamorphism occurred along the southern Central Asian Orogenic Belt (Li et al., 2013, 2016, 2017a). The WKO was amalgamated during closure of the Proto-Tethys Ocean between the active margin of the SKT and NKT during the Late Ordovician (Zhang et al., 2018c).

The middle Late Ordovician–late Silurian (450–428 Ma) represented the collisional orogenic stage (the third episode). During this period, the NKT and SKT underwent collision-related magmatism, N–S compression, and uplift of the Precambrian crystalline basement, including the formation of E–W-trending folded shear zones (Zhou et al., 2000). This third episode of orogenic contraction was related either to regional tectonics (e.g., the WKO; Xiao et al., 2005) or to a possible far-field connection to the amalgamation of the northern Tibetan Plateau and the Tarim Craton (Yin and Harrison, 2000).

Characterizing and identifying magmatic links between syn- and post-collisional processes remain challenging. Our detailed investigations in combination with an extensive regional analysis further refine the exact timing (450–428 Ma) of a major collision-related magmatic event during the closure of the Proto-Tethys Ocean and mountain-building along the OKQ suture zone. Our identification of collision-related granitoids from the eastern part of the WKO not only constrains when an arc/continent–continent collisional orogen ceased but also reveals a magmatic link, marked by high-Sr/Y or high-K geochemical characteristics, between syn- and post-collisional processes. During this episode, a distinct magmatic flare-up event is recognized, including coeval shoshonitic and adakitic magmatism (Wang et al., 2017), high-Ba–Sr appinite-granitoids (Ye et al., 2008), and coeval (436–440 Ma) mafic enclaves and dikes (Zhang et al., 2018a) distributed along the OKQ suture zone.

During the late Silurian–early Devonian (428–400 Ma), the post-orogenic episode was characterized by formation of A-type granitoids, coeval lamprophyre dikes, and highly evolved granitoids (Yuan et al.,

2002). This was associated with lithospheric thinning of the East Kunlun Orogen and adjacent areas (Meng et al., 2015), suggesting that the Kunlun Orogen became an area of regional extension. Magmatic activity during this stage was sparse, and the rocks are classified as high-K A-type granitoids (425–400 Ma) with strong negative Eu anomalies.

5.2. Petrogenesis and source nature of the Late Ordovician–middle Silurian magmatism

These distinct magmatic flare-up events are recorded by high-Sr/Y or high-K characteristic compositions. The high-Sr/Y (ALLK and YM) granitoids have high $(La/Yb)_N$ (mostly > 15) and Sr/Y (mostly > 40) ratios, and low HREE (Yb < 1.9 ppm) and Y (<18 ppm) contents, indicating geochemical characteristics of adakite-like rocks (Fig. 4C; Defant and Drummond, 1990). Their high-Sr/Y nature is in contrast to that of Cambrian–Middle Ordovician arc rocks in the area. Several recent petrogenetic models have been proposed to interpret the origin of adakite-like rocks, such as those examined in this study, including: (1) slab melting (Defant and Drummond, 1990); (2) partial melting of delaminated lower crust (Kay and Kay, 1993; Wang et al., 2006; Xu et al., 2002); (3) partial melting of thickened old lower crust (Chung et al., 2003; Zeng et al., 2011); (4) partial melting of thickened juvenile (newly formed) mafic lower crust (Li et al., 2017a); and (5) fractional crystallization of parental basaltic magmas with/without crustal assimilation (Castillo, 2012; Chiaradia, 2009; Macpherson, 2008).

The adakite-like rocks (high-Sr/Y granitoids) in the region contain the lower $\varepsilon_{Nd}(t)$ values (−2.4 to 1.3) and higher $(^{87}Sr/^{86}Sr)_i$ values (0.7055–0.7062), which is inconsistent with the features of typical adakitic rocks (Defant and Drummond, 1990). Moreover, the Late Ordovician ALLK rocks have high Sr/Y ratios, but low Mg#, Ni, and Cr contents, similar to those of adakites derived from thickened lower crust, rather than melts derived from subducted slab or those derived from delaminated lower crust (Fig. 3D; Wang et al., 2006). This is supported by their relatively lower $\varepsilon_{Nd}(t)$ values and higher $(^{87}Sr/^{86}Sr)_i$ values, in comparison with those of subducted oceanic crust adakites (Fig. 4D). Their relatively positive $\varepsilon_{Nd}(t)$ (0.8–1.4) and $\varepsilon_{Hf}(t)$ (7.2–12.1) values with young $T_{DM2}(Hf)$ ages (0.97–0.66 Ga) indicate a predominantly juvenile crustal source.

In contrast, the YM high-Sr/Y granitoids have high Mg#, Ni, and Cr contents similar to those of melts derived from delaminated lower crust, rather than melts derived from thickened lower crust (Fig. 4D). The negative $\varepsilon_{Nd}(t)$ (−2.4 to −2.3) values and $\varepsilon_{Hf}(t)$ (1.2–7.2) values with relatively old $T_{DM2}(Hf)$ ages (1.34–0.96 Ga) of these granitoids indicate a greater contribution of older crustal material with some mantle material to their source region (Fig. 6). The decoupled Hf–Nd isotopes of the high-Sr/Y YM granitoids have been explained by input of sediments or slab-derived melts rather than addition of slab fluids (Xu et al., 2017). This is because both HFSEs and REEs are relatively insoluble in hydrous fluids but are mobilized out of the subducted sediments or slab-derived melts (Class et al., 2000). Furthermore, these studied samples generally fall close to the different Pb isotopic compositions (Fig. 6C, D), also implying varied magma sources.

These high-K granitoids are mainly weakly peraluminous and belong to the high-K calc-alkaline and shoshonitic series (Fig. 4B). Furthermore, most samples plot in the magnesian fields, indicating that their compositional trends are similar to those of Caledonian-type post-collisional granitoids (Fig. S1). The sampled granitoids have mostly high contents of SiO_2 (> 72 wt.%) and K_2O (> 4.5 wt.%) and low abundances of MgO (< 0.7 wt.%), Cr, and Ni (Table S2), suggesting highly evolved magmas or crust-derived differentiated magmas. The high $(^{87}Sr/^{86}Sr)_i$ values (0.7060–0.7104), negative $\varepsilon_{Nd}(t)$ values (−7.7 to −2.1), and old two-stage Nd model ages (2.01–1.41 Ga) of these high-K granitoids suggest that their source contained an ancient crust component.

The Pb isotopic compositions of these high-K granitoids indicate a crustal melt source. The high-K granitoids also show Mg# values (11–42) higher than those expected for partial melts under crustal P–T conditions, suggesting that they are not pure crustal partial melts but also have minor mantle-derived magma input (Fig. 7). This hypothesis is corroborated by the Hf isotopic data [$\varepsilon_{Hf}(t) = -7.0$ to 11.9] and the two-model ages of 1.80–0.66 Ga. A mantle-derived component would explain the high magmatic temperatures and also account for some of the geochemical characteristics of these granitoids. The studied granitoids yield zircon saturation temperatures (T_{Zr}) of 732–820°C, except for three samples from the KDM pluton, which have high Zr contents (749–1020 ppm) and high T_{Zr} of 904–926°C (Watson and Harrison, 1983).

Furthermore, these high-Sr/Y granitoids are geochemically similar to adakites derived from thickened lower crust in southern Tibet and the Central Asian Orogen Belt (Fig. 5; Chung et al., 2003; Li et al., 2017a). Flat HREE patterns indicate the presence of amphibole-dominated residue in the source region. These high-K granitoids have mostly high

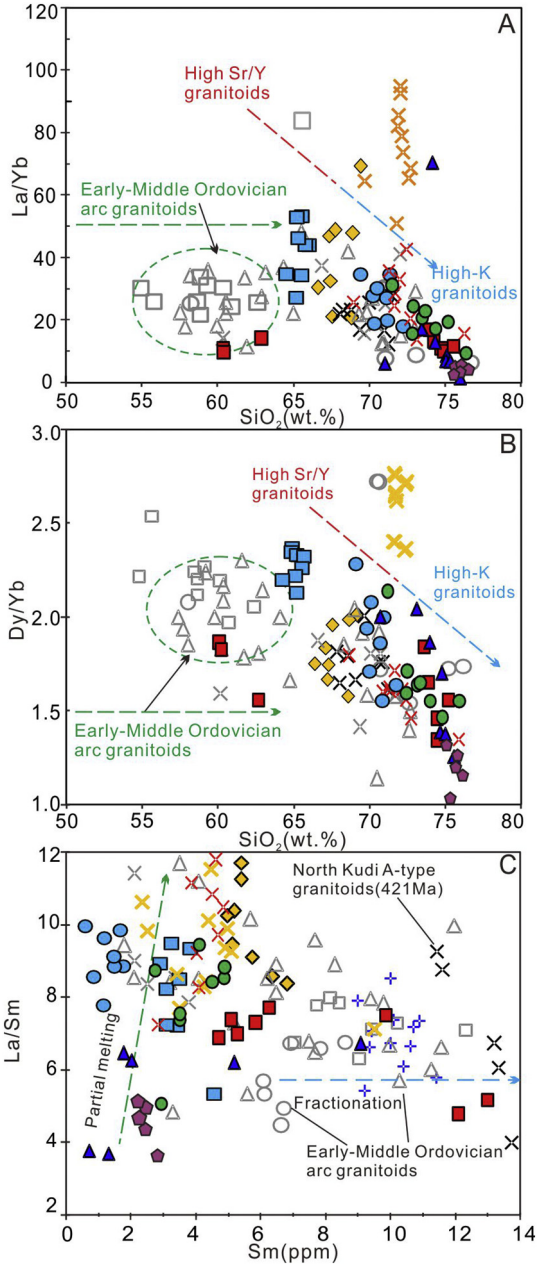

Fig. 7. (A) La/Yb vs. SiO_2, (B) Dy/Yb vs. SiO_2 (after Davidson et al., 2007), and (C) La/Sm vs. Sm diagrams for early Paleozoic granitoids in the West Kunlun orogenic belt, showing partial melting and fractionation trends. Symbols are as in Fig. 3.

HREE (Yb>1.9 ppm) and Y (>18 ppm) contents, low Sr/Y values, and strong negative Eu anomalies, and possess relatively flat HREE patterns (Fig. 5E), suggesting the stability field of plagioclase, with/without minor garnet as a residual phase. Moreover, these high-Sr/Y granitoids appear to show a trend from high La/Yb and Dy/Yb values in contrast to the high-K granitoids, indicating the presence of garnet and amphibole (Fig. 7).

These Late Ordovician–middle Silurian granitoids show variable Sr–Nd isotopic compositions with respect to SiO_2 (Fig. S1), which implies that crystal fractionation of these pure crustal melts, was not an important process following partial melting. The lack of correlation between initial Sr isotopic compositions and SiO_2 content (Fig. S1) also does not support crustal contamination or assimilation in these samples. Moreover, these granitoids show increasing La/Sm ratios with increasing Sm content, indicating that partial melting played an important role in magma genesis (Fig. 7). In contrast, Cambrian–Middle Ordovician granitoids in the area have similar low variation in La/Yb and Dy/Yb ratios with increasing SiO_2, consistent with differentiation from a mafic melt by olivine, clinopyroxene, and plagioclase (gabbroic) fractional crystallization (Li et al., 2017a; Fig. 7).

In summary, the distinct magmatic compositional diversity (from calc-alkaline through high-K calc-alkaline to shoshonitic) was produced during the flare-up period at 450-428 Ma. The compositional variations are associated with trace-element and Sr–Nd–Pb–Hf isotopic heterogeneities, thus pointing to multiple source regions involved in the magma genesis. The isotopic heterogeneities display signature characteristics of metasomatized regions in the continental lithospheric mantle, melts derived from delaminated lower crust, thickened juvenile mafic lower crust, and even the overlying continental crust (Freeburn, and Bouilhol1, P., Maunder, B., Magni, V., Hunen, J., 2017). We suggest that the mechanism driving such heterogeneities was slab break-off of Proto-Tethys oceanic slab.

5.3. Tectonic implications of Paleozoic slab break-off and crustal growth in NW Tibet

The occurrence of a magmatic flare-up event (metamorphism, migmatization, and mantle-derived magmatism) in an orogenic domain, long after the final emplacement of subduction-related magmas, and subsequently the closure of the oceanic basin, may be explained by several competing geodynamic models: (1) convective thinning of the lithospheric root (Houseman et al., 1981); (2) delamination due to the gravity-induced collapse of the orogenic root during late orogenic extension (Gardien et al., 1997); and (3) slab break-off affecting lithospheric structure in the orogenic belt (von Blanckenburg and Davies, 1995).

The Late Ordovician–middle Silurian magmatism in the WKO defines a new thermal event distinct from the subduction-related magmatism that terminated 10–15 Myr prior. These magmatic rocks are located within a belt ~40–80 km wide and ~1000 km long. The early Paleozoic magmatic belt-like shape of the “thermal anomaly” could be related to the existence of a narrow, linear, deeply rooted hot zone, which is typically produced by either subduction-related magmatism or slab break-off processes (von Blanckenburg and Davies, 1995). In contrast, convective thinning produces far more diffuse and widespread magmatic activity (Houseman et al., 1981). In the case of convective thinning, as the lithosphere is progressively heated from below, the lower boundary layer of the mechanical lithosphere melts, followed by melting of the shallower lithospheric mantle (Turner et al., 1999).

Decompression melting of the asthenosphere depends on the level to which the asthenosphere rises. Therefore, it is expected with a convective thinning model that the melting depth progressively decreases, and there is a transition in magma source from lithospheric mantle to asthenosphere (McKenzie and Bickle, 1988; Xu et al., 2008). However, the transition from Cambrian–Middle Ordovician subduction-related and calc-alkaline characteristic magmatism in the WKO (Yuan et al., 2002; Liao et al., 2010), rather than an enriched isotopic signature, to the Late Ordovician–middle Silurian magmatic activity under garnet-amphibolite-facies conditions (without an asthenosphere isotopic signature), is inconsistent with the convective thinning model.

Delamination would bring the asthenosphere into contact with the Moho as a result of the gravity-induced collapse of the orogenic root during late orogenic extension. This would induce intensive crustal melting and decompression melting of the asthenosphere if the crust is not very thick (Freeburn, and Bouilhol1, P., Maunder, B., Magni, V., Hunen, J., 2017; Turner et al., 1999). The Nd–Pb–Hf isotopic compositions of the studied magmatism (Fig. 6) further indicate predominant crustal melts with little mantle contribution under garnet-amphibolite-facies conditions, a feature inconsistent with delamination-induced crustal melting. The delamination process is expected to produce widespread, intensive asthenosphere-derived magmas (Davies and von Blanckenburg, 1995; Xu et al., 2008), which are rarely recognized in the WKO. Hence, the delamination model seems inappropriate for explaining the Late Ordovician–middle Silurian magmatic regime in the WKO.

In the slab break-off model, oceanic slab detachment allows the asthenosphere beneath the subducting plate to flow into the broken slab window above the sinking slab. The heat supply from the underlying asthenosphere can affect the overriding lithosphere, yielding diverse magmatism, such as melting and/or metamorphism (Fig. 9). Asthenosphere upwelling induces partial melting of the overlying lithospheric mantle previously metasomatized during subduction. Thermal flux can cause crustal melting, leading to crustal components within mantle-derived melts through AFC (assimilation and fractional crytallization) processes (Xu et al., 2008). Hence, the slab break-off model predicts a magmatic evolution pattern similar to that envisaged by the convective thinning model. However, unlike the diffusive and widespread pattern in the convective thinning case, slab detachment predicts a narrow, linear zone of magmatism of limited extent, similar to what we observe in the WKO.

Late Ordovician–middle Silurian post-collisional magmatism in the WKO has previously been attributed to slab break-off, especially magma derived from partial melting of the continental crust and sediments (Freeburn, and Bouilhol1, P., Maunder, B., Magni, V., Hunen, J., 2017; von Blanckenburg and Davies, 1995). With respect to the Cambrian–Middle Ordovician arc granitoid plutons, the development of magmatic activity at 450–428 Ma in the WKO, as well as coeval gabbroic dikes and appinites along the OKQ suture zone, is most likely the consequence of partial melting of differing magma source regions (Figs. 8 and 9). These source regions include overriding continental crust and minor lithospheric mantle, through increasing the temperature of the lithosphere and decreasing the pressure of the asthenosphere after slab break-off (Fig. 9). This has also been observed in the Mediterranean–Carpathian region (Coulon et al., 2002; Davies and von Blanckenburg, 1995; Van de Zedde and Wortel, 2001) and in southern Tibet during the magmatic flare-up period (Chung et al., 2003). This style of magmatism is therefore considered typical of heterogeneous compositions. This interpretation is consistent with numerical modeling that indicates that hot asthenosphere continues to ascend and generate melt for several million years after slab break-off (Van Hunen and Allen, 2011).

After initial collision of the NKT (Tarim Block) and SKT, asthenosphere upwelling could have been triggered by the subducted Proto-Tethys slab break-off. The small-scale and short-term nature of Late Ordovician–middle Silurian magmatism is in stark contrast to the characteristics of delamination (large-scale) and/or convective thinning (long-term) (Xu et al., 2008). Thus, the favored mechanism for Late Ordovician–middle Silurian magmatism in the WKO is slab break-off involving Proto-Tethys oceanic lithosphere (Fig. 9).

The Proto-Tethys oceanic slab break-off model is preferred over other models on account of other geological evidence/observations in the region:

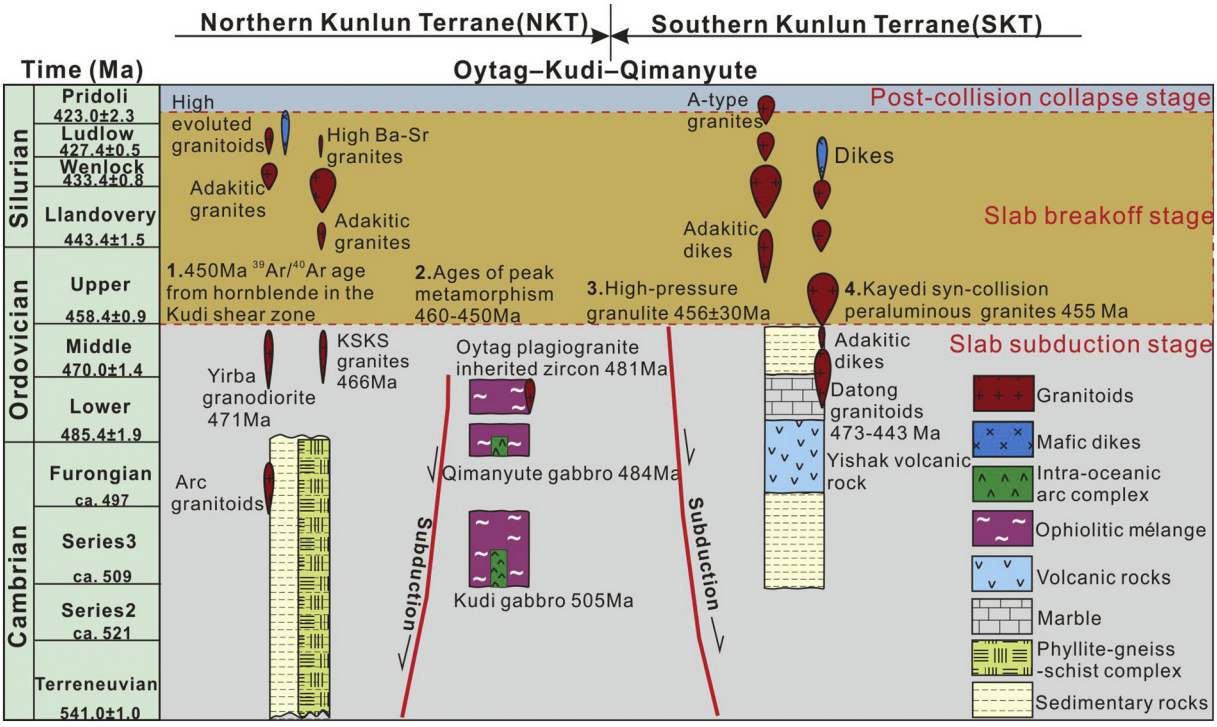

Fig. 8. Space–time diagram demonstrating the spatial and tectonic relationships among the tectono stratigraphic units of the West Kunlun orogenic belt (based on our own work and modified after Xiao et al., 2005; Jiang et al., 2008; Zhang et al., 2018b, 2018c, 2018d).

(1) The termination of Proto-Tethys arc magmatism (Zhang et al., 2018a): Since arc-related magmatism stopped at~455 Ma, calc-alkaline igneous rocks have not been emplaced in the WKO. Minor ~455 Ma syn-collisional S-type magmatism during this period was derived from a metasedimentary-dominated source within the middle–upper crust, marking the termination of oceanic lithosphere subduction.

(2) Thermal metamorphism (e.g., DeCelles et al., 2002; Kohn and Parkinson, 2002): The thermal flux resulting from the asthenosphere ascending through the slab window causes metamorphism (Mahéo et al., 2002). This is documented in the WKO metamorphic record (e.g., Wang, 2008; Ye et al., 2008). Wang (2008) investigated high-pressure granulite-facies metamorphic rocks in the Taxkorgan area, which were metamorphosed under high pressure during the Ordovician. A similar peak in metamorphism was identified by Ye et al. (2008) by collating all existing metamorphic ages in the WKO.

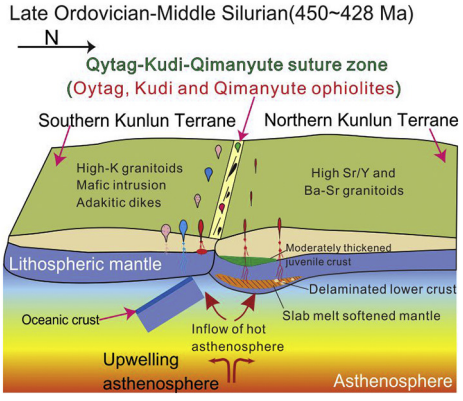

Fig. 9. Schematic tectonic diagrams showing tectono-magmatic evolution along the Oytag–Kudi–Qimanyute suture zone in the West Kunlun orogenic belt.

(3)The magmatic units in WKO from pre-455 Ma (subduction-related rocks) and post-455 Ma (collisional-related magmatic rocks) are geochemically distinct: Most of the pre-455 Ma magmas in the WKO are characterized by positive ε_{Nd} values, high Mg#, and low SiO_2 content (<62 wt.%), and are classified as metaluminous and calc-alkaline. The post-455 Ma magmas, however, are characterized by high potassium contents, high Sr/Y, negative ε_{Nd}, low Mg#, and high SiO_2 content (> 62 wt. %), and are mostly peraluminous (Figs. 4, 6, and S1). The pre-455 Ma magmas were likely related to subduction of the Proto-Tethys oceanic plate underneath the SKT. The nature and composition of post-455 Ma magmas differ markedly from those corresponding to the pre-455 Ma history of convergence zones. This magmatic evolution suggests that a change in magmatic conditions is commonly induced by oceanic slab break-off.

This Paleozoic period (450–428 Ma), during which slab break-off occurred in the WKO and coincided with Late Ordovician–middle Silurian magmatism, is undoubtedly an important milestone in Earth's history (e.g., Li et al., 2017b). The generation of linear magmatic activity (high-Sr/Y and high-K plutons, minor gabbroic dikes) with the return of high-pressure rocks to the surface along the OKQ suture zone defines the onset of post-collisional processes in the WKO along the northwestern margin of the Tibetan Plateau.

The Tibetan Plateau, the largest uplifted structure on Earth, is considered to have formed in response to the India–Asia collision. The orogen underwent a series of collisions, where by crustal terranes were successively accreted to the southern margin of Eurasia during the transition of the Proto-, Palaeo-, and Neo-Tethys oceans (Yin and Harrison, 2000; Xiao et al., 2002, 2005; Yin, 2010; Cao et al., 2015). Our study provides a rare insight into orogenic systems that currently exist along the northwestern margin of the Tibetan Plateau, especially in the Tethys domain orogenic belt (Li et al., 2017b; Xiao et al., 2002, 2005). There are distinct similarities to other orogenic-evolution and mountain-building processes, such as in the Himalayan–Tibetan orogen, the Alps, and the Central Asian Orogenic Belt. This study also provides a template for

magmatic diversity as a response to slab break-off, related to the growth of continental crust after oceanic closure along collision zones.

Some Late Ordovician–middle Silurian high-Sr/Y granitoids along the OKQ suture zone have high $\varepsilon_{Nd}(t)$ (−2.4 to +1.3) and zircon $\varepsilon_{Hf}(t)$ (+1.2 to +12.1) values, recording significant crustal growth by addition of juvenile magma generated from remnants of the subducted oceanic slab, but with some crustal recycling (Fig 6). This suggests that juvenile crustal growth in the older orogenic systems that occurs by arc addition also involves some vertical addition and crustal recycling during the final stage of orogenic collision. To some extent, this is probably similar to the Cenozoic syn-collisional rocks from southern Tibet, the Mesozoic syn-collisional rocks from the North and South Qilian Orogenic Belts, and the East and West Kunlun Orogenic Belts (Huang et al., 2014; Kong et al., 2018; Niu et al., 2013; Zhang et al., 2016c). Our study therefore provides a rare insight into older orogenic systems, suggesting that this neoteric hypothesis is feasible.

6. Conclusions

We have presented the first identification of Late Ordovician–middle Silurian granitoids with high-Sr/Y or high-K along the OKQ suture zone in the eastern West Kunlun Orogen. They occur along the northwestern margin of the Tibetan Plateau, and their emplacement is dated at 450–428 Ma. With respect to Cambrian–Middle Ordovician subduction-related granitoids, these high-Sr/Y and high-K granitoids show that there was a change in tectonic setting during the Late Ordovician–middle Silurian. This change was likely a transition from a waning continental arc to an initial collision and slab break-off, and it initiated magma generation under garnet-amphibolite-facies conditions along the OKQ suture zone. This distinct magmatic flare-up event is most likely the consequence of partial melting of differing magma sources through increasing lithospheric temperature and decreasing pressure of the asthenosphere after slab break-off. The WKO is thus a prime example of heterogeneous flare-up magmatism, with signature high-Sr/Y and high-K characteristics, where continental crustal growth occurred in response to slab break-off.

Supplementary data to this article can be found online at https://doi.org/10.1016/j.lithos.2019.07.014.

Acknowledgements

We thank Dr. Andrew Kerr for his constructive suggestions and comments. We are also grateful to Ke-Jun Hou and Qing-Qing Zhao for their assistance with LA–ICP–MS zircon U–Pb dating, and to Gui-Bin Zhang for his assistance with measurements of zircon Hf isotopes. Dr. Li Shan, Dr. He Zhenyu, Prof. Dong Shuwen, and Dr. Wang Rui also gave helpful suggestions. Thanks are due to two anonymous reviewers for their comments that helped to improve the manuscript. This study was funded by the Strategic Priority Research Program of Chinese Academy of Sciences, Grant No. XDA20070304, the Fundamental Research Funds for the Chinese Academy of Geological Sciences (YYWF201601, JKY1723), projects of China Geological Survey (DD20190367, 20160083-1, 12120115000801, 121201101000150014), and the National Natural Science Foundation of China (41772232, U1603245). The work is a contribution to IGCP 662.

References

Barbarin, B., 1999. A review of the relationships between granitoid types, their origins and their geodynamic environments. Lithos 46 (3), 605–626.
Cao, K., Wang, G.C., van der Beek, M., Bernet, P., Zhang, K.X., 2015. Exhumation history of the West Kunlun Mountains, northwestern Tibet: evidence for a long-lived, rejuvenated orogen. Earth Planet. Sci. Lett. 432 (15), 391–403.
Castillo, P.R., 2012. Adakite petrogenesis. Lithos 134–135, 304–316.
Chiaradia, M., 2009. Adakite-like magmas from fractional crystallization and melting-assimilation of mafic lower crust (Eocene Macuchi arc, Western Cordillera, Ecuador). Chem. Geol. 265 (3-4), 468–487.
Chung, S.L., Liu, D.J., Ji, M.F., Chu, H.Y., Lee, D.J., Wen, C.H., Lo, T.Y., Lee, Q.Q., Zhang, Q., 2003. Adakites from continental collision zones: melting of thickened lower crust beneath southern Tibet. Geology 31 (11), 1021–1024.
Class, C., Miller, D.M., Goldstein, S.L., Langmuir, C.H., 2000. Distinguishing melt and fluid subduction components in Umnak Volcanics, Aleutian arc. Geochem. Geophys. Geosyst. 1. https://doi.org/10.1029/1999GC000010 (1999GC00010).
Coulon, C., Megartsi, M., Fourcade, S., Maury, R.C., Bellon, H., Louni-Hacini, A., Cotten, J., Coutelle, A., Hermitte, D., 2002. Post-collisional transition from calc–alkaline to alkaline volcanism during the Neogene in Oranie (Algeria): magmatic expression of a slab breakoff. Lithos 62 (3-4), 87–110.
Davidson, J.S., Turner, H., Handley, C., Macpherson, Dosseto, A., 2007. Amphibole "sponge" in arc crust? Geology 35 (9), 787–790.
Davies, J.H., von Blanckenburg, F., 1995. Slab breakoff: a model of lithosphere detachment and its test in the magmatism and deformation of collisional orogens. Earth Planet. Sci. Lett. 129 (1-4), 85–102.
DeCelles, P.G., Robinson, D.M., Zandt, G., 2002. Implications of shortening in the Himalayan fold-thrust belt for uplift of the Tibetan Plateau. Tectonics, 21 https://doi.org/10.1029/2001TC001322.
Defant, M.J., Drummond, M.S., 1990. Derivation of some modern arc magmas by melting of young subducted lithosphere. Nature 347, 662–665.
Dewey, J.F., Shackleton, R., Chang, C.F., 1988. The tectonic evolution of the Tibetan Plateau: philosophical transactions of the royal society of London. Ser. A 327 (1), 379–413.
Fang, A.M., Li, J.L., Liu, X.H., Hou, Q.L., Lee, I.J., Xiao, W.J., Yu, L.J., Zhou, H., 2003. Tectonic settings of the basic igneous rocks in the Kudi ophiolite zone of West Kunlun Mountains, Xinjiang Province. Acta Petrol. Sin. 19, 409–417 (in Chinese with English abstract).
Freeburn, R., Bouilholl, P., Maunder, B., Magni, V., Hunen, J., 2017. Numerical models of the magmatic processes induced by slab breakoff. Earth Planet. Sci. Lett. 478 (15), 203–213.
Frost, B.R., Frost, C.D., 2008. A geochemical classification for feldspathic igneous rocks. J. Petrol. 49 (11), 1955–1969.
Gardien, V., Lardeaux, J.M., Ledru, P., 1997. Metamorphism during late orogenic extension: insights from the French Variscan belt. Bull. Soc. Geol. Fr. 168, 271–286.
Han, F.L., Cui, J.T., Ji, W.H., Li, H.P., Hao, J.W., 2002. Discovery of the Qimanyute ophiolite in the Western Kunlun and its geological significance. Geol. Bull. China 21, 573–578 (in Chinese with English abstract).
Hou, K.J., Li, Y.H., Tian, Y.Y., 2009. In situ U-Pb zircon dating using laser ablation-multi ion counting-ICP-MS. Mineral. Deposita 28 (4), 481–492 (in Chinese with English abstract).
Houseman, G.A., McKenzie, D.P., Molnar, P., 1981. Convective instability of a thickened bondary layer and its relevance for the thermal evolution of continental convergent belts. J. Geophys. Res. 86 (B7), 6115–6132.
Hsü, K., Pan, G.T., Sengör, A., 1995. Tectonic evolution of the Tibetan Plateau: a working hypothesis based on the archipelago model of orogenesis. Int. Geol. Rev. 37 (6), 473–508.
Huang, H., Niu, Y.L., Nowell, G., Zhao, Z.D., Yu, X.H., Zhu, D.C., Ding, S., 2014. Geochemical constraints on the petrogenesis of granitoids in the East Kunlun Orogenic belt, northern Tibetan Plateau: implications for continental crust growth through syn-collisional felsic magmatism. Chem. Geol. 370 (2014), 1–18.
Ji, W.H., Hang, F.L., Wang, J.C., Zhang, J.L., 2004. Composition and geochemistry of Subashi ophiolitic mélange in the West Kunlun and its geological significance. Geol. Bull. China 1196–1201 (in Chinese with English abstract).
Ji, W.Q., Wu, F.Y., Chung, S.L., Wang, X.C., Liu, C.Z., Li, Q.L., Liu, Z.C., Liu, X.C., Wang, J.G., 2016. Eocene Neo-Tethyan slab breakoff constrained by 45 Ma oceanic island basalt–type magmatism in southern Tibet. Geology 44 (4), 283–286.
Jia, R.Y., Jiang, Y.H., Liu, Z., Zhao, P., Zhou, Q., 2013. Petrogenesis and tectonic implications of early Silurian high-K calc-alkaline granites and their potassic microgranular enclaves, western Kunlun orogen, NW Tibetan Plateau. Int. Geol. Rev. 55 (8), 958–975.
Jiang, Y.H., Liao, S.Y., Yang, W.Z., Shen, W.Z., 2008. An island arc origin of plagiogranites at Oytag, western Kunlun orogen, northwest China: SHRIMP zircon U–Pb chronology, elemental and Sr– Nd–Hf isotopic geochemistry and Paleozoic tectonic implications. Lithos 106 (3-4), 323–335.
Jiang, Y.H., Jia, R.Y., Liu, Z., Liao, S.Y., Zhao, P., Zhou, Q., 2013. Origin of middle Triassic high–K calc–alkaline granitoids and their potassic microgranular enclaves from the western Kunlun orogen, northwest China: a record of the closure of Paleo–Tethys. Lithos 156–159, 13–30.
Kay, R.W., Kay, S.M., 1993. Delamination and delamination magmatism. Tectonophysics 219 (1-3), 177–189.
Kohn, M.J., Parkinson, C.D., 2002. Petrologic case for Eocene slab breakoff during the Indo-Asian collision. Geology 30, 591–594.
Kong, J.J., Niu, Y.L., Duan, M., Shao, F.L., Xiao, Y.Y., Zhang, Y., Guo, P.Y., Sun, P., Gong, H.M., 2018. The syncollisional granitoid magmatism and crust growth during the West Qinling Orogeny, China: insights from the Jiaochangba pluton. Geol. J. 1–20. https://doi.org/10.1002/gj.3368.
Li, S., Wang, T., Wilde, S.A., Tong, Y., 2013. Evolution, source and tectonic significance of early Mesozoic granitoid magmatism in the central Asian Orogenic Belt (central segment). Earth-Sci. Rev. 126, 206–234.
Li, S., Chung, S.-L., Wilde, S.A., Wang, T., Xiao, W.-J., Guo, Q.-Q., 2016. Linking magmatism with collision in an accretionary orogen. Sci. Rep. 6, 25751.
Li, S., Chung, S.L., Wilde, S.A., Jahn, B.M., Xiao, W.J., Wang, T., Guo, Q.Q., 2017a. Early-middle Triassic high Sr/Y granitoids in the southern central Asian Orogenic Belt: implications for ocean closure in accretionary orogens. J. Geophys. Res. 122 (6), 2291–2309.

Li, S.Z., Zhao, S.J., Liu, X., Cao, H.H., Yu, S., Li, X.Y., Somerville, I., Yu, S.Y., Suo, Y.H., 2017b. Closure of the Proto-Tethys Ocean and early Paleozoic amalgamation of microcontinental blocks in East Asia. Earth-Sci. Rev. https://doi.org/10.1016/j.earscirev.2017.01.011 in press.
Liao, S.Y., Jiang, Y.H., Jiang, S.Y., Yang, W.Z., Zhou, Q., Jin, G.D., Zhao, P., 2010. Subducting sediment-derived arc granitoids: evidence from the Datong pluton and its quenched enclaves in the western Kunlun orogen, northwest China. Mineral. Petrol. 100 (1-2), 55–74.
Liu, Z., Jiang, Y.H., Jia, R.Y., Zhao, P., Zhou, Q., Wang, G.C., Ni, C.Y., 2014. Origin of middle Cambrian and late Silurian potassic granitoids from the western Kunlun orogen, northwest China: a magmatic response to the Proto-Tethys evolution. Mineral. Petrol. 108 (1), 91–110.
Liu, Z., Jiang, Y.H., Jia, R.Y., Zhao, P., Zhou, Q., 2015. Origin of late Triassic high–K calcalkaline granitoids and their potassic microgranular enclaves from the western Tibet Plateau, northwest China: implications for Paleo–Tethys evolution. Gondwana Res. 27, 326–341.
Ludwig, K.R., 2003. User's Manual for Isoplot 3.00: A Geochronological Toolkit for Microsoft Excel. vol. 4. Berkeley Geochronology Center Special Publication, pp. 1–70.
Macpherson, C.G., 2008. Lithosphere erosion and crustal growth in subduction zones: insights from initiation of the nascent East Philippine Arc. Geology 36 (4), 311–314.
Mahéo, G., Guillot, S., Blichert-Toft, J., Rolland, Y., Pecher, A., 2002. A slab breakoff model for the Neogene thermal evolution of South Karakorum and South Tibet. Earth Planet. Sci. Lett. 195 (1-2), 45–58.
Maniar, P.D., Piccoli, P.M., 1989. Tectonic discrimination of granitoids. Geol. Soc. Am. Bull. 101, 635–643.
Martin, H., Smithies, R.H., Rapp, R., Moyen, J.F., Champion, D., 2005. An overview of adakite, tonalite-trondhjemite-granodiorite (TTG), and sanukitoid: relationships and some implications for crustal evolution. Lithos 79 (1-2), 1–24.
Matte, P., Tapponnier, P., Arnaud, N., Bourjot, L., Avouac, J.P., Vidal, P., Qing, L., Pan, Y.S., Yi, W., 1996. Tectonics of Western Tibet, between the Tarim and the Indus. Earth Planet. Sci. Lett. 142 (3-4), 311–330.
Mattern, F., Schneider, W., 2000. Suturing of the Proto-and Paleo-Tethys oceans in the western Kunlun (Xinjiang, China). J. Asian Earth Sci. 18 (6), 637–650.
McKenzie, D.P., Bickle, M.J., 1988. The volume and composition of melt generated by extension of the lithosphere. J. Petrol. 29 (3), 625–679.
Meng, F.C., Cui, M.H., Wu, X.K., 2015. Heishan mafic-ultramafic rocks in the Qimantag area of Eastern Kunlun, NW China: remnants of an early Paleozoic incipient Island arc. Gondwana Res. 27 (2), 745–759.
Middlemost, E.A.K., 1994. Naming materials in the magma/igneous rock system. Earth Sci. Rev. 37 (3-4), 215–224.
Niu, Y.L., Zhao, Z.D., Zhu, D.C., Mo, X.X., 2013. Continental collision zones are primary sites for net continental crust growth-A testable hypothesis. Earth-Sci. Rev. 127 (2013), 96–110.
Pan, Y.S., Wang, Y., 1994. Discovery and evidence of the fifth suture zone of Qinghai– Tibetan Plateau. Acta Geophys. Sin. 37 (2), 241–250 (in Chinese with English abstract).
Patiño Douce, A.E., Johnston, A.D., 1991. Phase equilibria and melt productivity in the pelitic system: implications for the origin of peraluminous granitoids and aluminous granulites. Contrib. Mineral. Petrol. 107 (2), 202–218.
Paton, C., Hellstrom, J., Paul, B., Woodhead, J., Hergt, J., 2011. Iolite: freeware for the visualisation and processing of mass spectrometric data. J. Anal. At. Spectrom. https://doi.org/10.1039/c1ja10172b.
Peccerillo, A., Taylor, S.R., 1976. Geochemistry of Eocene calc-alkaline volcanic rocks from the Kastamonu area, Northern Turkey. Contrib. Mineral. Petrol. 58 (1), 63–81.
Petford, N., Atherton, M., 1996. Na-rich partial melts from newly underplated basaltic crust: the Cordillera Blanca Batholith, Peru. J. Petrol. 37 (6), 1491–1521.
Rapp, R.P., Watson, E.B., 1995. Dehydration melting of metabasalt at 8–32 kbar: implications for continental growth and crust–mantle recycling. J. Petrol. 36 (4), 891–931.
Richards, J.P., Kerrich, R., 2007. Special paper: Adakite-like rocks: their diverse origins and questionable role in metallogenesis. Econ. Geol. 102, 537–576.
Sisson, T.W., Ratajeski, K., Hankins, W.B., Glazner, A.F., 2005. Voluminous granitic magmas from common basaltic sources. Contrib. Mineral. Petrol. 148 (6), 635–661.
Sun, S.S., McDonough, W.F., 1989. Chemical and isotopic systematics of oceanic basalts: implications for mantle composition and processes. Geol. Soc. Lond. Spec. Publ. 42 (1), 313–345.
Turner, S.P., Platt, J.P., George, R.M.M., Kelley, S.P., Pearson, D.G., Novew, G.M., 1999. Magmatism associated with orogenic collapse of the Betic-Alboran domain, SE Spain. J. Petrol. 40 (6), 1011–1036.
Van de Zedde, D.M.A., Wortel, M.J.R., 2001. Shallow slab detachment as a transient source of heat at midlithospheric depths. Tectonics 20 (6), 868–882.
Van Hunen, J., Allen, M.B., 2011. Continental collision and slab break-off: a com-parison of 3-D numerical models with observations. Earth Planet. Sci. Lett. 302 (1-2), 27–37.
Von Blanckenburg, F., Davies, J.H., 1995. Slab breakoff: a model for syncollisional magmatism and tectonics in the Alps. Tectonics 14 (1), 120–131.
Wang, Z.H., 2004. Tectonic evolution of the western Kunlun orogenic belt, western China. J. Asian Earth Sci. 24 (2), 153–161.
Wang, J.P., 2008. Geological features and tectonic significance of melange zone in the Taxkorgan area, West Kunlun. Geol. Bull. China 27 (12), 2057–2066 (in Chinese with English abstract).
Wang, J.C., Han, F.L., Cui, J.T., Zhang, J.L., 2003. Geochemical characteristics of early Paleozoic granites in the Pulu area, Yutian, Xinjiang and its tectonic significance. Geol. Bull. China 22, 170–183 (in Chinese with English abstract).
Wang, Q., Xu, J.F., Jian, P., Bao, Z.W., Zhao, Z.H., Li, C.F., Xiong, X.L., Ma, J.L., 2006. Petrogenesis of adakitic porphyries in an extensional tectonic setting, Dexing, South China: implications for the genesis of porphyry copper mineralization. J. Petrol. 47 (1), 119–144.
Wang, C., Liu, L., He, S.P., Li, R.S., Yang, W.Q., Cao, Y.T., Zhu, X.H., Li, R.S., 2013. Early Paleozoic magmatism in west Kunlun: constraints from geochemical and zircon U-Pb-Hf isotopic studies of the Bulong granite. Chin. J. Geol. 48, 997–1014 (in Chinese with English abstract).
Wang, R., Collins, W.J., Weinberg, R.F., Li, J.X., Li, Q.Y., He, W.Y., Richards, J.P., Hou, Z.Q., Zhou, L.M., 2016. Xenoliths in ultrapotassic volcanic rocks in the Lhasa Block: direct evidence for crust-mantle mixing and metamorphism in the deep crust. Contrib. Mineral. Petrol. 172, 62. https://doi.org/10.1007/s00410-016-1272-6.
Wang, J., Hattori, K., Liu, J.G., Song, Y., Gao, Y.B., Zhang, H., 2017. Shoshonitic- and adakitic magmatism of the early Paleozoic age in the Western Kunlun orogenic belt, NW China: implications for the early evolution of the northwestern Tibetan plateau. Lithos 286–287, 345–362.
Wang, R., Weinberg, R.F., Collins, W.J., Richards, J.P., Zhu, D.C., 2018. Origin of post-collisional magmas and formation of porphyry Cu deposits in southern Tibet. Earth-Sci. Rev. 181, 122–143.
Watson, E.B., Harrison, T.M., 1983. Zircon saturation revisited: temperature and composition effects in a variety of crustal magma types. Earth Planet. Sci. Lett. 64 (2), 295–304.
Wu, F.Y., Yang, Y.H., Xie, L.W., Yang, J.H., Xu, P., 2006. Hf isotopic compostions of the standard zircons and baddeleyites used in U–Pb geochronology. Chem. Geol. 234 (1-2), 105–126.
Xiao, W.J., Windley, B.F., Hao, J., 2002. Arc-ophiolite obduction in the western Kunlun range (China): implications for the Paleozoic evolution of central Asia. J. Geol. Soc. Lond. 159 (5), 517–528.
Xiao, X.C., Wang, J., Su, L., Song, S.G., 2003. A further discussion of the Küda ophiolite, West Kunlun, and its tectonic significance. Geol. Rev. 22 (10), 745–750 (in Chinese with English abstract).
Xiao, W.J., Windley, B.F., Liu, D.Y., Jian, P., Liu, C.Z., Yuan, C., Sun, M., 2005. Accretionary tectonics of the Western Kunlun Orogen, China: a Paleozoic–Early Mesozoic, long-lived active continental margin with implications for the growth of Southern Eurasia. J. Geol. 113 (6), 687–705.
Xu, J.F., Shinjo, R., Defant, M.J., Wang, Q., Rapp, R.P., 2002. Origin of Mesozoic adakitic intrusive rocks in the Ningzhen area of east China: partial melting of delaminated lower continental crust? Geology 30 (12), 1111–1114.
Xu, Y.G., Lan, J.B., Yang, Q.J., Huang, X.L., Qiu, H.N., 2008. Eocene breakoff of the Neo-Tethyan slab as inferred from intraplate-type mafic dykes in the Gaoligong orogenic belt, eastern Tibet. Chem. Geol. 255 (3-4), 439–453.
Xu, Y., Liu, C.Z., Chen, Y., Guo, S., Wang, J.G., Sein, K., 2017. Petrogenesis and tectonic implications of gabbro and plagiogranite intrusions in mantle peridotites of the Myitkyina ophiolite, Myanmar. Lithos 284–285, 180–193.
Yang, J.S., Robinson, R.T., Jiang, C.F., Xu, Z.Q., 1996. Ophiolites of the Kunlun Shan, China and their tectonic implications. Tectonophysics 258, 215–231.
Ye, H.M., Li, X.H., Li, Z.X., Zhang, C.L., 2008. Age and origin of high Ba–Sr appinite–granites at the northwestern margin of the Tibet Plateau: implications for early Paleozoic tectonic evolution of the Western Kunlun orogenic belt. Gondwana Res. 13 (1), 126–138.
Yin, A., 2010. Cenozoic tectonic evolution of Asia: a preliminary synthesis. Tectonophysics 488 (1-4), 293–325.
Yin, A., Harrison, T.M., 2000. Geologic evolution of the Himalayan–Tibetan orogen. Annu. Rev. Earth Planet. Sci. 28, 211–280.
Yuan, C., Sun, M., Zhou, M.F., Zhou, H., Xiao, W.J., Li, J.L., 2002. Tectonic evolution of the Western Kunlun: geochronologic and geochemical constraints from Kudi granites. Int. Geol. Rev. 44 (7), 653–669.
Yuan, C., Sun, M., Zhou, M.F., Xiao, W.J., Zhou, H., 2005. Geochemistry and petrogenesis of the Yishak Volcanic Sequence, Kudi ophiolite, West Kunlun (NW China): implications for the magmatic evolution in a subduction zone environment. Contrib. Mineral. Petrol. 150, 195–211.
Zartman, R.E., Doe, B.R., 1981. Plumbotectonics–the model. Tectonophysics 75 (1-2), 135–162.
Zeng, L.S., Gao, L.E., Xie, K.J., Liu, Z.J., 2011. Mid-Eocene high Sr/Y granites in the Northern Himalayan Gneiss Domes: melting thickened lower continental crust. Earth Planet. Sci. Lett. 303 (3-4), 251–266.
Zhang, C.L., Li, H.K., Zou, H.B., 2013. Tectonic framework and evolution of the Tarim Block in NW China. Gondwana Res. 23, 1306–1315.
Zhang, Q.C., Liu, Y., Huang, H., Wu, Z.H., Zhou, Q., 2016a. Petrogenesis and tectonic implications of the high-K Alamas calc-alkaline granitoids at the northwestern margin of the Tibetan Plateau: geochemical and Sr–Nd–Hf–O isotope constraints. J. Asian Earth Sci. 127 (2016), 137–151.
Zhang, G.B., Ireland, T., Zhang, L.F., Gao, Z., Song, S.G., 2016b. Zircon geochemistry of two contrasting types of eclogite: implications for the tectonic evolution of the North Qaidam UHPM belt, northern Tibet. Gondwana Res. 35 (2016), 27–39.
Zhang, Y., Niu, Y.L., Hu, Y., Liu, J.J., Ye, L., Kong, J.J., Duan, M., 2016c. The syncollisional granitoid magmatism and continental crustal growth in the West Kunlun Orogen, China—evidence from geochronology and geochemistry of the Arkarz pluton. Lithos 245 (2016), 191–204.
Zhang, Q.C., Wu, Z.H., Li, S., Li, K., Liu, Z.W., Zhou, Q., 2018a. Origin of Ordovician granitoids and their Silurian mafic dikes from the western Kunlun orogen, northwest China: implications for evolution of the Proto-Tethys. Acta Geol. Sin. 93, 30–49 ((English Edition), Accept).
Zhang, C.L., Zou, H.B., Ye, X.T., Chen, X.Y., 2018b. Timing of subduction initiation in the Proto-Tethys Ocean: evidence from the Cambrian gabbros from the NE Pamir Plateau. Lithos 314–315, 40–51.

Zhang, C.L., Zou, H.B., Ye, X.T., Chen, X.Y., 2018c. Tectonic evolution of the NE section of the Pamir Plateau: new evidences from field observation and zircon U-Pb geochronology. Tectonophysics 723 (2018), 27–40.
Zhang, C.L., Zou, H.B., Ye, X.T., Chen, X.Y., 2018d. Tectonic evolution of the West Kunlun Orogenic Belt along the northern margin of the Tibetan Plateau: Implications for the assembly of the Tarim terrane to Gondwana. Geosci. Front. 10, 973–988.
Zhou, H., Chu, Z.Y., Li, J.L., Hou, Q.L., Wang, Z.H., Fang, A.M., 2000. 40Ar /39Ar dating of ductile shear zone in Kudi, West Kunlun, Xinjian. Sci. Geol. Sin. 35 (2), 233–239 (in Chinese with English abstract).